INTERNATIONAL JOURNAL FOR NUMERICAL METHODS IN FLUIDS, VOL. 10, 519–555 (1990)

LARGE EDDY SIMULATION OF A DEVELOPING TURBULENT BOUNDARY LAYER AT A LOW REYNOLDS NUMBER

H. M. TSAI AND D. C. LESLIE

The Turbulence Unit in the School of Engineering, Queen Mary College, London E1 4NS, U.K.

SUMMARY

A spectral code has been used to simulate a developing turbulent boundary layer at low Reynolds number Re_θ (based on free stream velocity and momentum thickness) between 353 and 576. The starting field was generated by allowing a step change of temperature to diffuse outwards from one wall in a fully developed channel flow. The thermal boundary layer so created was conditionally sampled to convert it into a momentum boundary layer with an irrotational free stream region, a process which is justified by appeal to experiments. This initial field was allowed to develop until the momentum boundary layer thickness δ_{995} had grown to about 1·5 times its original thickness.

The results of the simulation have been compared with a wide range of experimental data. The outcome of this comparison is generally very satisfactory; the main trends of the experiments are well reproduced and our simulation supplements and extends the existing sets of experimental data. The simulation also gives pressure statistics which cannot be obtained experimentally. In particular, it gives the contribution of pressure diffusion to the balance equations for the Reynolds stress and indicates the error produced by omitting this term.

KEY WORDS Simulation Large eddy simulation Turbulence Boundary layer Developing flows

1. INTRODUCTION

This paper reports a large eddy simulation (LES) at low Reynolds number of a nominally two-dimensional, incompressible homogeneous turbulent boundary layer developing in time under zero pressure gradient.

There is now considerable experience of the simulation of free and wall-bounded turbulent shear layers using both full and large eddy simulation. Examples of free shear layer simulations are the work of Mansour *et al.*,[1] Riley and Metcalfe[2] and Cain *et al.*[3] for turbulent mixing layers and of Orszag and Pao[4] and Riley and Metcalfe[5] for turbulent wakes. Except for the work of Mansour *et al.*,[1] all these were done using full simulation. Mansour *et al.* demonstrated the feasibility of treating intermittently turbulent flow fields using LES. Channel flows have been studied using synthetic[6,7] and natural (no-slip) boundary conditions.[8–11]

Experience in simulating boundary layers is comparatively limited. Spalart[12] has studied a boundary layer undergoing transition, while Spalart and Leonard[13] and Spalart[14] have reported work on turbulent equilibrium boundary and sink flow boundary layers respectively.

0271–2091/90/050519–37$18.50

Received July 1988
Revised April 1989

These are full simulation studies and like the present work are at low Reynolds numbers. Large eddy simulations of turbulent boundary layers known to the authors are by Friedrich and Su[15] and Schmitt *et al.*[16] The former studied a spatially developing boundary layer with longitudinal curvature. Both used synthetic boundary conditions with their inherent limitation in the representation of the solid wall.

The present work utilizes the LES experience of Moin and Kim in wall-bounded flows using natural boundary conditions and that of Mansour *et al.* in free shear layers to study a turbulent boundary layer, which has features of both these flows. Spalart's simulation was full, while this study relies on LES.

Spalart simulated a boundary layer which is stationary in time and growing in the streamwise direction; he used a similarity transform to make this flow compatible with his code, which uses periodic boundary conditions in the streamwise direction. We have preferred to postulate homogeneity in the streamwise direction, so that the boundary conditions in this direction are truly periodic, and to assume that the layer is growing outwards from the plate as time evolves. This model ignores certain effects due to the streamwise growth. This approximation is admissible since the rate of growth of the layer thickness with downstream distance is small (of order 0·015); in particular, the results are statistically stationary in a frame of reference which moves with the flow. Although this use of periodic boundary conditions reproduces most of the features of the flow, the spatially averaged mean velocity component normal to the flow direction is zero. This renders the mean streamlines parallel to the direction of flow, in contrast to the inclination found in a spatially developing flow, but it does not imply that there is no entrainment or lateral growth in the simulated flow; the layer grows in time. A flow which is statistically steady but non-homogeneous in the streamwise direction is therefore transformed into one which is statistically homogeneous in the streamwise direction but time-dependent. This transformation provides a major numerical simplification.

The current simulation is in fact of a homogeneous boundary layer formed by the sudden constant motion of one of the two walls in its own plane. This layer is one-dimensional and develops in time. The resemblance to a spatially developing boundary layer is, as we shall see, good. Wray *et al.*[17] have used this approximation for their investigation of the instability of a laminar boundary layer, and other investigators have done the same.

The choice of using natural boundary conditions with limitation of computing resources has confined us to the lowest Reynolds numbers at which the boundary layer is truly turbulent. Using $16 \times 33 \times 64$ spectral modes, a reasonable simulation can be made for a range of Reynolds number Re_θ, based on momentum thickness θ, from 353 to 576. Extensions to somewhat higher Reynolds numbers would be possible with more modes; a substantial extension would demand the use of some kind of synthetic boundary conditions.

Experimental results and analysis of low-Reynolds-number boundary layers have been reported in (among others) References 18–23. Mean velocity profiles and some turbulent quantities were measured. The most detailed measurements are those by Murlis *et al.*,[22] who reported third-order velocity products, energy balances and conditionally sampled results; these are for Reynolds numbers substantially higher than those simulated in the present study. Flow visualizations made by Falco[24,25] and Head and Bandyopadhyay[26] give qualitative pictures of some important features of the layer. Owing to the limitations of existing experimental methods, only some aspects of the flow dynamics can be studied. A detailed knowledge of all the instantaneous primitive variables in the entire flow can only come from a simulation.

A summary of the numerical scheme is given in Section 2. In Section 3 the use of periodic boundary conditions is justified and also the resolution requirements are discussed. The procedure for generating an appropriate initial field to start the computation is described in Section 4. In Section 5–9 the results are presented.

2. NUMERICAL MODELS AND SIMULATION CODE

The simulations have all been made with the code BUOYAN-77. This is an updated version of the QMC Turbulence Unit's original channel code CHANEL.[10,27,28] The later code is much faster than the earlier one and has been rewritten in FORTRAN-77 by Mr. K. A. Cliffe of AERE, Harwell; also it incorporates a scalar field, a facility which was used in this study, but only to generate the starting field. Results for a developing thermal layer were taken at the same time and these will be reported elsewhere.

The CHANEL family of codes is fully spectral. Fourier expansion is used in the streamwise (x) and spanwise (z) directions, implying periodicity in these directions; a Chebyshev expansion is used in the y-direction. The modal structure defines a grid of collocation points; much of the computation, including the evaluation of the subgrid model described below, is done in configuration space on this grid.

The grid-scale Navier–Stokes equations may be written

$$\frac{\partial u_i}{\partial t} = -\frac{\partial p}{\partial x_i} + \nu \frac{\partial^2 u_i}{\partial x_i^2} + S_i, \qquad \frac{\partial u_i}{\partial x_i} = 0, \tag{1}$$

where S_i contains the non-linear and subgrid terms. This 'historic' term is so called because it is treated explicitly (Adam–Bashforth) while the pressure and molecular viscous terms are handled implicitly (Crank–Nicholson). As we shall consider later, the subgrid eddy viscosity is small in the present simulation compared to the molecular viscosity.

Fourier transformation reduces (1) to a set of uncoupled linear equations in the new-time variables. u, w and p can then be eliminated to give a fourth-order equation in v only; in CHANEL and its descendents, this equation is solved by Chebyshev expansion. This procedure has a strong resemblance to the projective method originated by Leray[29] and applied in this context by (for example) Leonard and Wray.[30] p can then be calculated algebraically, and finally, two further second-order equations are solved for u and w. Further details are found in Reference 27. Note that in this paper the direction perpendicular to the wall is y rather than z as used in the original code; this is to conform to engineering usage, where y often refers to the direction of shear.

In the original code, which was designed for channel flows, the boundary conditions are that u, v and w should be zero on both walls. In the boundary layer simulation this condition is retained for the lower (hàrd) wall. On the upper wall v and w are again zero, but u is fixed at the free stream velocity. This choice is discussed further in Section 4.

The subgrid model used here is very similar to that of Moin and Kim.[9] Following Schumann,[7] Moin and Kim modelled the subgrid term in two separate parts, the isotropic and the inhomogeneous (anisotropic) part. The separation is effected by averaging over planes parallel to the wall. Denoting this operation by $\langle\ \rangle$, the model is

$$\tau_{ij} = -\nu_t(S_{ij} - \langle S_{ij}\rangle) - \nu_t^* \langle S_{ij}\rangle. \tag{2}$$

The first term on the right-hand side is the isotropic and the second the inhomogeneous part, with

$$S_{ij} = \frac{1}{2}\left(\frac{\partial u_i}{\partial u_j} + \frac{\partial u_j}{\partial u_i}\right),$$

$$\nu_t = l_1^2[2(S_{ij} - \langle S_{ij}\rangle)(S_{ij} - \langle S_{ij}\rangle)]^{1/2},$$

$$\nu_t^* = l_2^2(2\langle S_{ij}\rangle\langle S_{ij}\rangle)^{1/2},$$

$$l_1 = c_1\Delta[1 - \exp(-y^+/A)],$$

$$l_2 = c_2\Delta^*[1 - \exp(-y^{+2}/A^2)],$$

$$\Delta = (\Delta_1\Delta_2\Delta_3)^{1/3} \quad \text{and} \quad \Delta^* = \Delta_3.$$

The constant A in the damping factor was set at 25, while the subgrid scale constants c_1 and c_2 were 0·1 and 0·5 respectively. These values have been confirmed by extensive simulations of channel flow. y^+ ($\equiv yu_\tau/\nu$) is the non-dimensionalized vertical distance from the wall, u_τ being the local wall friction velocity. The Δ_i are the distances between the collocation points. In contrast to Moin and Kim,[9] prefiltering was not used and so the collocation grid determines the effective length scale. It is only for this reason that our subgrid scale model constants appear to differ from theirs; the two sets are equivalent.

As noted, these models have been validated in simulations of channel flow by the QMC Turbulence Unit. They have not been altered in any way for this boundary layer study. In particular, no special treatment of any form was employed to handle the turbulent/non-turbulent interface. Even in the outer free stream the subgrid scale models were allowed to operate, though in such an irrotational field their contributions will be negligibly small. The only minor difference is that the value of y^+ used in the damping factor varies in time as the plane-averaged wall friction velocity decreases in a developing boundary layer. u_τ was therefore calculated at each time step and used to update the damping factors.

Note that in a high-Reynolds-number LES the molecular dissipation will be small, and without a subgrid model the overall dissipation would be much too low. Often the subgrid contributions dominate. However, here, since the simulation is at low Reynolds number, the role of the subgrid models in dissipation is considerably less than that of the molecular viscosity. Their role is nonetheless crucial. Since the demands on the model are small, one cannot conclude from its success here that the models would necessarily be adequate at higher Reynolds numbers.

3. BOUNDARY CONDITIONS, RESOLUTION REQUIREMENTS AND COMPUTATIONAL DETAILS

The spatial extent of the large-scale structure is typically some boundary layer thicknesses. Here the two-point velocity correlation measurements of Grant[31] and Tritton[32] can be used as a guide. Roughly speaking, the largest significant structures would be of the order of the separation at which the correlations tail to zero. The experimental streamwise and spanwise correlations go to zero at separation distances of approximately $1{\cdot}5\delta$ and δ respectively. However, these correlations are for an Re_θ of 1800, which is much larger than that of the flow in which we are interested. These correlation lengths might be significantly different at low Re_θ, though there is no firm evidence of this. The correlations do not seem to depend on the Reynolds number in turbulent channel flows (compare the results of Moin and Kim[9] and Moser[33] with those of Comte-Bellot[34]). This suggests that it is more likely that in boundary layers the correlations are similarly behaved; lacking adequate information, we assume that this is the case.

To avoid interference with the largest eddies and to ensure that the energy-containing eddies are fully represented, it would seem correct to make the periodic computational box at least twice as big as the correlation length. Our box size is identical to that used in our channel simulations (at Re similar to the present work), namely $2\pi h \times 2h \times \pi h$,[10] h being the half-width between the two walls. With an initial boundary layer thickness of approximately h, the box is therefore more than adequate. The maximum permissible boundary layer thickness should thus be fixed by

$$3\delta < 2\pi h, \qquad 2\delta < \pi h.$$

The second conditions is the more restrictive and implies $\delta < 1{\cdot}5h$. The simulation was in fact terminated when the boundary layer had grown to this thickness.

One must of course ask whether this is sufficient, i.e. whether the outcome of the simulation is affected by the finite size of the box. The evidence presented in Section 7 is reasonably encourag-

ing on this point. In the near-wall region the correlations do fall to reasonably low values at maximum separation. They do not do so at the edge of the boundary layer, but this can reasonably be ascribed to the intermittent presence of non-turbulent fluid.

The use of periodic boundary conditions for the spanwise direction is acceptable since the flow is homogeneous in that direction. For the streamwise direction, homogeneity can only be an approximation. Turbulent boundary layers developing at zero pressure gradient grow at a streamwise rate $d\delta/dx$ of approximately 0·015. The outer edge of the layer therefore subtends an angle of approximately 1° with the horizontal. The streamwise non-homogeneity is therefore small compared to the vertical scale of inhomogeneity, and the properties of the simulated homogeneous boundary layer will be very close to those of a boundary layer which grows in the streamwise direction.

A summary of the specifications for the simulation is given in Table I. The parameters are for the initial field; the dimensions in wall units change with time as u_τ decreases.

The computations were performed on the CRAY-1S of the University of London Computer Centre. This has 1 Mword of fast store and, since there is no SSD (solid state device), the computation must remain in the fast memory. The fast Fourier transforms built into the code restrict the number of modes to be a power of 2 in every direction (strictly, 2^N+1 for the Chebyshev polynomials in the y-direction); since 18 fields must be stored for each mode triad, the maximum problem which can be handled is $2^{15} = 576$ kwords. Experimentation has shown that 64 modes are necessary in the spanwise (z) direction; 32 are not enough to resolve the near-wall rollers. Thanks to the strong stretching provided by the Chebyshev polynomials near the wall, 33 modes suffice in the cross-stream (y) direction. This leaves only 16 for the streamwise direction (x). We would have preferred to use more, but the results presented below show that 16 is marginally sufficient. The fact that the numbers of modes are in the ratio 1:2:4 is a coincidence.

4. INITIAL FIELD GENERATION

To start the computation, the computational domain must be initialized with some appropriate velocity field. The only absolute requirement is that the numerical scheme must be able to converge from this starting field to the appropriate stationary state. Provided this requirement is met and the process is stationary, then the simulation must succeed. It is still desirable to specify the starting field well, since this will reduce the computing time needed to pass from the initial state to a statistically stationary condition.

In their turbulent channel flow studies, Moin *et al.*[8] used an initial field with a component from the solution of the Orr–Sommerfeld equation and superimposed upon it a mean flow and some random perturbations. The Orr–Sommerfeld equation introduces the necessary large structures in the flow. Others prefer to generate a pseudo-random field with the right mean and RMS

Table I. Resolution details of the computational box used. Note that the sizes in wall units refer to the initial field. They decrease as the flow develops in the computation

	x	y	z
Box size (physical)	$2\pi h$	$2h$	πh
Box size (wall units)	1219	388	609
Number of modes	16	33	64
Mesh size (wall units)	76	0·93 (min)	9·5

values[6,7] or with the higher sophistication, of introducing the Reynolds stress as well.[10] The higher the order of sophistication the less computation will be required before the flow settles to a statistically stationary state.

Orszag and Pao[4] started their simulation of a momentumless wake with a simple procedure using a random number generator, but the fields do not show any Reynolds stresses or third-order statistics. The demarcation between a turbulent/non-turbulent regime is therefore not clear. Using this field for their simulation of a tow wake, Riley and Metcalfe[5] observed an initial long lag period in the development of the wake, during which the various second and third-order statistics developed while there was little change in the overall size of the wake. During this adjustment period, there is little decay of energy as the large eddies develop and give rise to the higher-order statistics. This work was done in a full simulation study; it is likely that if subgrid scale models were used, the flow would laminarize.

It appears that for a mixing layer the initial conditions are more sensitive in determining the subsequent development of the flow, even after a long streamwise distance, than for other turbulent shear flows.[35,36] Therefore care must be taken not to introduce any artificial modes in simulation studies. In the case of the boundary layer, this is happily not too critical. Experiments show that the initial Tollmein–Schlichting disturbances quickly break up into three-dimensional structures. It is therefore likely that even if the initial large structures are unrealistic, they will evolve into their natural modes. However, one constraint in the present study is that the simulation time is much shorter than is needed for this evolution to be fully realized. It follows that the simulation cannot succeed unless the starting field is quite close to reality.

The method adopted here is relatively simple. The initial field used is the hot region of the field of a thermal layer developing from the suddenly heated wall of a fully developed turbulent channel flow as calculated by LES. To create this, a developed channel simulation with uniform temperature from a previous study[10] was used. One of the walls was impulsively heated: this resulted in the formation of an internal thermal layer developing in a flow which is already fully turbulent. The field was allowed to develop in time until the mean thermal layer thickness was approximately half the channel width. The thermal layer then has a convoluted structure and turbulent statistics not dissimilar to that found in a turbulent boundary layer. Experimental evidence for this can be found in the work of Dean and Bradshaw[37] for flow at high Reynolds number in a duct, and the flow visualization work of Head and Bandyopadhyay[26] on turbulent boundary layers at a Reynolds number very much lower and comparable to ours.

Using conditionally sampled data, Dean and Bradshaw demonstrated that the layer developing from one wall in a duct flow has turbulence characteristics very similar to those of an isolated boundary layer spreading into a non-turbulent free stream with the same mean velocity as the duct flow. They inferred that, to a first approximation, the duct flow could be regarded as the superposition of two boundary-layer-like wall flows. Conversely, a wall-type flow could be extracted from a duct or channel flow if we could find some method of unscrambling the overlapping. This proposition is crucial to our approach, and we shall therefore review the evidence for it in some detail.

Dean and Bradshaw applied heat as a tracer to one of the boundary layers at the entry region of a duct, before it starts to interact with the upper layer; they then tracked its subsequent behaviour as the two layers merge. The general conclusion is that downstream of the merging of the opposite shear layers in a turbulent duct flow, the large-scale eddies erupting from one side of the centreline time-share with those from the opposite side. Although Dean and Bradshaw's experimental situation is not identical with our use of fully developed channel flow, much of the basic idea is similar. In the present case the large-scale structures erupting from one wall were tagged by heating this wall.

Head and Bandyopadhyay injected smoke below a turbulent boundary layer from the wall region, thus creating an internal layer contaminated with smoke. The visualization offered by the smoke reveals well developed vortex motion with unmistakable vortex pairs (hairpins), very similar to those found when the entire boundary layer (at low Re_θ) was filled with smoke. Their experiment was at a low Re_θ of about 500, comparable to our present work. The eddies from the wall region marked by the smoke evolved to become the dominant eddies in the boundary layer: these are responsible for the distortion of the surface dividing the turbulent/non-turbulent regions. It is these eddies that constitute the initial field structures for the present boundary layer simulation.

To capture these structures of the hot internal layer, a simple conditional sampling algorithm was used. The internal layer was discriminated by means of the temperature level. Where the temperature exceeded the free stream value by an amount T_H, the intermittency function was set to unity, otherwise it was zero. A threshold value was necessary since there is a small variation of the temperature in the free stream owing to the numerical rounding errors. The value of T_H was set rather arbitrarily to approximately twice the RMS value of the temperature in the free stream. The intermittency profile thus generated is shown in Figure 1: it is much flatter than the experimental profile. It is likely that this is due at least in part to the additional viscous contribution from the subgrid eddy viscosity, which makes the superlayer thicker and less well defined. The profile would therefore be critically dependent on the threshold setting, and this is what is found here. A scheme more sophisticated than one based on only threshold setting would render the intermittency less threshold-dependent,[38] but for the present purpose a simple scheme suffices.

In the hot region the planar-averaged intermittency γ is appreciably different from zero; here the velocity is unmodified if the local intermittency function is unity, while if it is zero the velocities are set equal to the planar averages. In the whole of the cold region, including the upper boundary, u is set to the free stream value and v, w to zero; there are no fluctuations. The field so generated does not satisfy continuity; it is made divergence-free by taking a small time step. The properties of this starting field will be described later.

In this study we allow the field to develop under zero pressure gradient. It is likely that the initial field retains some favourable pressure gradient effects since it originates from a channel flow driven by a pressure gradient. However, at the Reynolds numbers with which we are working, these effects should die off quickly since the hairpin structures which dominate the entire

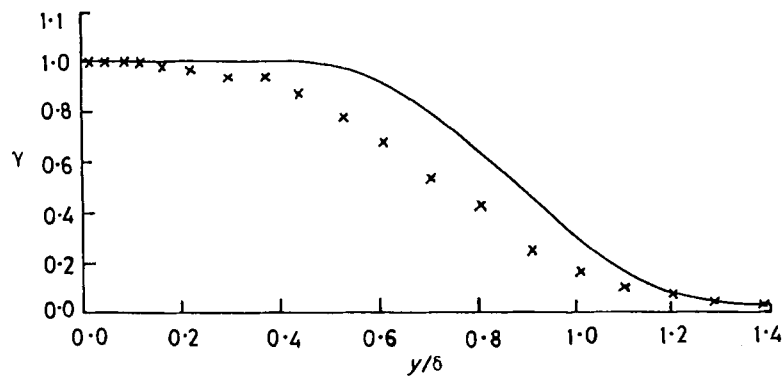

Figure. 1. Intermittency profile of the initial field $Re_\theta = 353$: ——, experimental data from Reference 22; ×, present computation

boundary layer at these Reynolds numbers have a shorter life span than those large structures whose make-up is different at larger Reynolds number.

The calculation starts from a dump of a fully developed turbulent channel flow at $hu_\tau/\nu = 194$, corresponding to a half-width and mean velocity Reynolds number of about 3200. This dump comes from a previous simulation of the experiment of Kreplin and Eckelmann[39] which has constant (zero) temperature throughout. A brief account of this simulation is given by Gavrilakis *et al.*[10] and full details will be presented elsewhere. When the simulation has been restarted from the dump, the temperature of the lower wall is impulsively increased from zero to unity (the precise value is of course arbitrary). A thermal boundary layer starts to grow from this wall, and the conditional sampling process described above is applied when the thermal layer thickness has grown to approximately the channel half-width h; the Re_θ value of the velocity boundary layer so generated is 353.

5. MEAN FLOW QUANTITIES

Using the initial field described above, the flow was allowed to evolve over a non-dimensional time $32{\cdot}6h/U_e$, h and U_e being the semi-width of the computational domain and the free stream velocity respectively. At the end of this period the boundary layer thickness δ had grown to $(3/2)h$, at which point the influence of the top wall must be becoming significant, and Re_θ has increased to 576. Statistics have been taken for the initial and final values of Re_θ and at the intermediate values 396, 434, 471 and 505.

The development of characteristic mean parameters of the flow with time is shown in Figure 2. The values of δ^*/δ_{995} and θ/δ_{995} are approximately 1/7 and 1/10 respectively, in good agreement with a host of experimental results. These and all other statistics are taken by averaging over a plane parallel to the wall and also over a short time interval $0{\cdot}093h/U_e$ centred on the time in question. This second averaging gives some additional smoothing, but there is still considerable scatter in most of our statistical data and especially in the higher-order statistics. Nonetheless, trends are visible and are sufficient to provide a good picture of the turbulent flow processes.

It would of course be desirable if the scatter could be reduced, but the only certain way of doing this for a non-stationary process is to repeat the simulation with a number of different starting fields. Perhaps at least 10 re-runs would be needed to give any worthwhile reduction in scatter, and we have not been able to afford this. One could of course use a similarity hypothesis to combine data for differing Re_θ. However, this method would defeat one of our objectives, which is to establish whether the flow does in fact evolve in a self-similar way: therefore we have not used it.

Assuming the convective velocity to be the same as the free stream velocity, the equivalent downstream distance x' in a spatially growing boundary layer at each successive time station can be worked out. The rate of growth of the boundary layer thickness δ_{995} is approximately 0·016 (from Figure 2), which is consistent with the normal development of a boundary layer at zero pressure gradient. This agreement is fortuitious since x' is intimately linked with the value of the convective velocity used. The mean free stream velocity is not necessarily the correct one to use: it is likely that the convective velocity should be less than this. Sternberg[40] estimated the convection velocity for the large-scale structures to be approximately 25% greater than the local mean velocity in the near-wall region and approximately 25% lower then the mean velocity in the outer region. If this is correct, the simulated rate of growth of the boundary layer is larger than the experimental value. This could be explained by the fact that the contribution of the eddy viscosity effectively increases the viscous superlayer thickness and thus the entrainment rate. Note that at this low Re_θ the hairpin vortices are of the same order as the boundary layer thickness and they

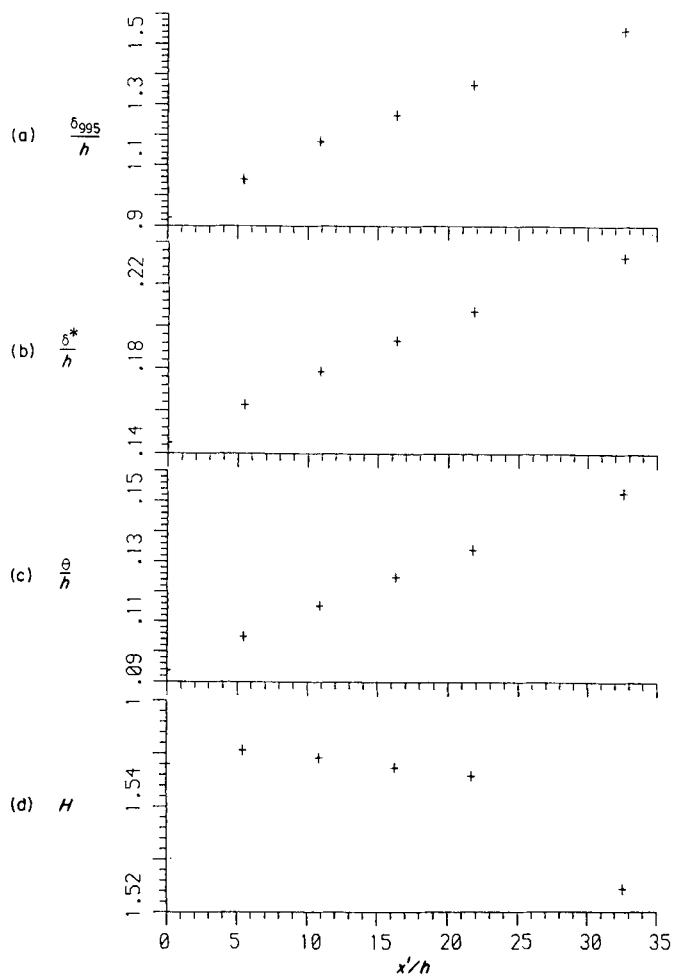

Figure 2. Variation of (a) boundary layer thickness, (b) displacement thickness, (c) momentum thickness and (d) shape factor with streamwise distance $x' \equiv U_e t^*$

control the process of entrainment.[26] As Moin and Kim[41] demonstrated, the use of LES would increase the scale of the hairpins simulated. It is therefore not surprising that the rate of boundary layer growth is somewhat overestimated. In general, provided the scales of these hairpins are adequately resolved, this additional contribution to the entrainment should not be too significant.

A more revealing way to assess the various parameters is to examine their variation with Reynolds number. Figures 3 and 4 show the variation of the shape factor H and the skin friction coefficient C_f, with Reynolds number. As in the experimental measurements, $H \simeq 1{\cdot}3$–$1{\cdot}6$, decreasing as Re_θ increases. The values of the shape factor measured by Purtell *et al.*[21] and those of the current simulation (Figure 3) fall between Coles' relation for H and that of Landweber.[42] C_f is evaluated using the derivative of the mean velocity on the wall. The extent to which the present computed values of C_f fall within the range of experimental data is good (Figure 4), though the rate of decrease of the simulated C_f with Re_θ is higher than that given by experiment.

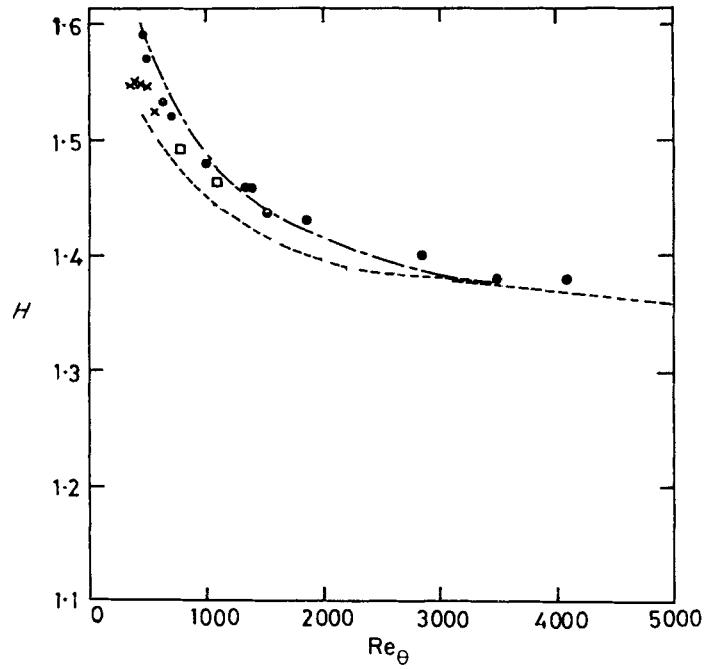

Figure 3. Variation of shape factor H with Re_θ: ×, present computations; ●, Reference 21; ○, Reference 26; □, Reference 22; – – –, Reference 18; ——— ———, Reference 42

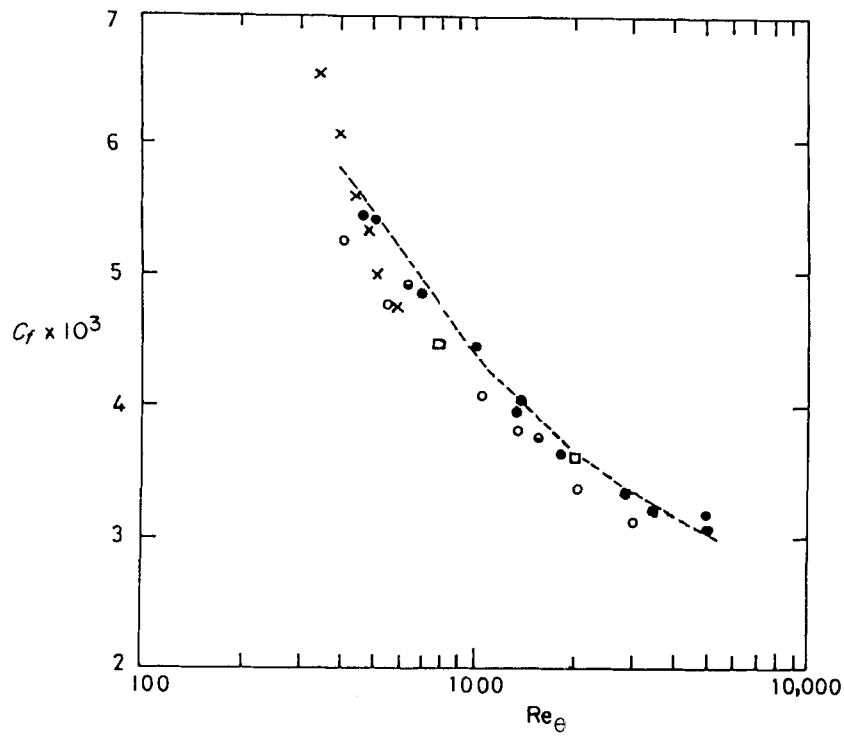

Figure 4. Variation of skin friction coefficient with Re_θ: symbols are as in Figure 3

When the mean streamwise velocity is plotted against the usual non-dimensionalized distance y^+, a substantial logarithmic region is found for all Re_θ. The first mesh point away from the wall was located at $y^+ \leqslant 1{\cdot}0$. With five collocation points, the viscous sublayer is well represented. The computed mean velocity profiles indicate this and correspond very well with the curve $U^+ = y^+$ represented by the broken line in Figure 5. As is well known, the mean velocity profile deviates from this linear region at $y^+ > 8$, and the current computations show this.

However, the fit to the usual logarithmic law

$$u^+ = \frac{1}{\kappa} \ln y^+ + C, \quad \kappa = 0{\cdot}4, \quad C = 5{\cdot}2, \tag{3}$$

is poor. Figure 5 shows a semi-logarithmic plot of the data for

$$\kappa = 0{\cdot}37, \quad C = 4{\cdot}5. \tag{4}$$

The fit is good at the three highest values of Re_θ (471, 505 and 576) but is less so at the start of the computation. Notice that at $Re_\theta = 471$, x'/δ is approximately 18 and this corresponds to about one large eddy turnover time. A reasonable inference is that history effects have more or less died out towards the end of the computation.

There is of course much debate as to whether the constants in equation (3) should be Reynolds-number-dependent. Huffman and Bradshaw[20] and Purtell *et al.*[21] argued that they

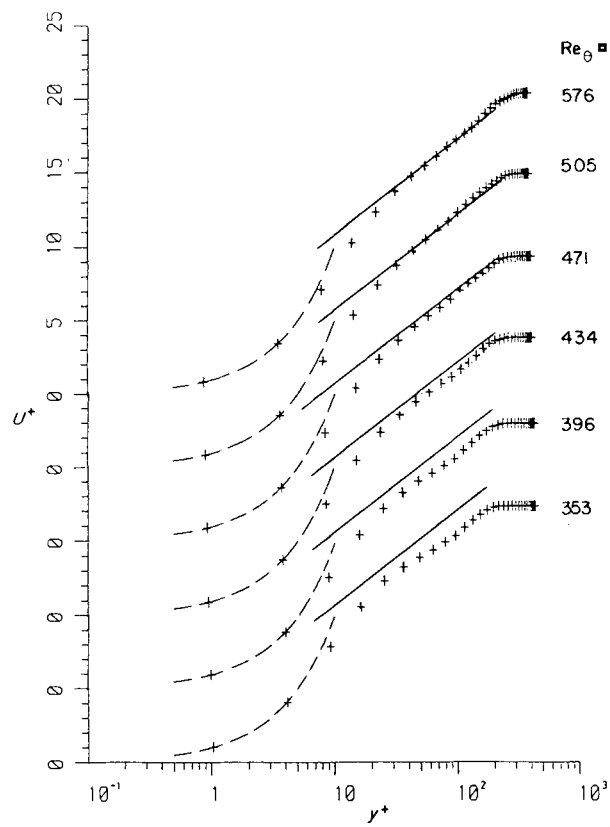

Figure 5. Mean velocity profiles in wall co-ordinates (note shifted origins for each successive curve): ——, law of the wall with $\kappa = 0{\cdot}37$, $C = 4{\cdot}5$; – – –, $U^+ = y^+$.

should not. On the other hand, the values in (4) agree much better than do those in (3) with the low-Reynolds-number channel experiments of Eckelmann.[43] The values in (4) are reproduced exactly by the channel simulation from which the present simulation was started; it is striking that the present simulation initially deviates from them and then returns to them as history effects die out. Note that the wake component is also formed as Re_θ increases. Further discussion of the developmental state of the boundary layer will be given below when we consider the wake region, where, as Klebanoff and Diehl showed,[44] underdevelopment will be principally reflected.

Spalart (Reference 14, Figure 4) finds that equation (3) fits his simulation very well when the acceleration parameter K is $1{\cdot}5 \times 10^{-6}$; the fit is less good for $K = 2{\cdot}5 \times 10^{-6}$. The difference between the two formulae is not great (equation (4) is 1·4% higher for $y^+ = 100$) and in view of the proven effect of K one would not expect our mean velocity profile to agree precisely with Spalart's.

Since the simulation was started with a slightly artificial initial field, an assessment of the subsequent state of the layer is important. Although the state of the flow at the various stages of evolution is interesting, we need to determine which of the various profiles show full development: following Coles,[18] this is defined as a state independent of the route by which it is derived. Thus different initial fields could be used which would create different downstream boundary layer development, but they may all finally arrive at the same fully developed state if appropriate similarity variables are used. The similarity profile of the mean velocity, plotted as U/U_e against y/δ_{995} in Figure 6, shows that the profiles do not show any noticeable deviation, except for the initial field ($Re_\theta = 353$) where the values of U/U_e are slightly lower in the centre of the boundary layer. Since underdevelopment would, as noted above, mainly be seen in the outer region, we could infer that of the six profiles shown, all but that for $Re_\theta = 353$ are fully developed. Plotted in this fashion, the differences in the profiles are less striking than those in Figure 5. It is likely that

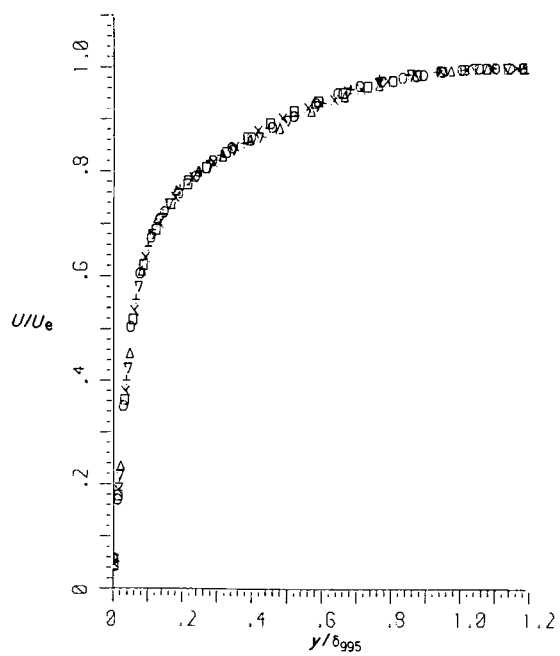

Figure 6. U/U_e versus y/δ_{995}: △, $Re_\theta = 353$; ▽, 396; +, 434; ×, 471; □, 505; ○, 576

the latter gives a more stringent indication of, and emphasizes another aspect of, the developmental state of the flow.

In the outer region the mean velocity may be represented by

$$u^+ = \frac{1}{\kappa} \ln y^+ + C + \frac{\Pi}{\kappa} w(y/\delta), \tag{5}$$

where w and Π are the wake function and wake parameter respectively. The third term on the right-hand side of equation (5) gives the deviation from the log law. The wake function Π is defined so as to satisfy the conditions $w(1) = 2$ and $w(0) = 0$. The maximum deviation from the log law, $\Delta U^+ \equiv 2\Pi/\kappa$, characterizes the strength of the wake. We use the logarithmic law of equation (4), which is a good fit to the present results, to determine this deviation: its dependence on Re_θ is shown in Figure 7. Also included is Coles' proposed best fit to the then available experimental data. The wealth of experimental data suggests that $2\Pi/\kappa$ reaches a value 2·8 for $Re_\theta > 5000$. Mabey[45] found that this parameter reaches a maximum at $Re_\theta \simeq 6000$ before decreasing slowly with further increase in Reynolds number.

In the range of Re_θ of interest here, the wake component rises quite sharply with Re_θ. From Coles' tabulation the wake would disappear at $Re_\theta = 465$. Careful checks of this by Purtell *et al.*, and also the recent measurements of Castro,[46] indicate that this is not necessarily so. Our computation of $2\Pi/\kappa$ shows the appropriate upward trend with increasing Re_θ: its magnitude agrees well with the curve suggested by Coles' experimental tabulation. Any underdevelopment of these fields would, as pointed out by Coles, show up as a pronounced deviation from the curve: the points from the underdeveloped profiles of Purtell *et al.* plotted in Figure 7 shows this. Only three points from the present results are plotted here since the rest are small or zero. Note that Π is a geometric parameter and it is possible for it to be negative even when the flow is fully developed.

6. TURBULENT QUANTITIES

The subgrid contribution to the Reynolds stress follows directly from the subgrid models, but the estimation of this contribution to the other quantities is highly speculative. Most of the results presented are therefore the contributions from the grid-scale motion only.

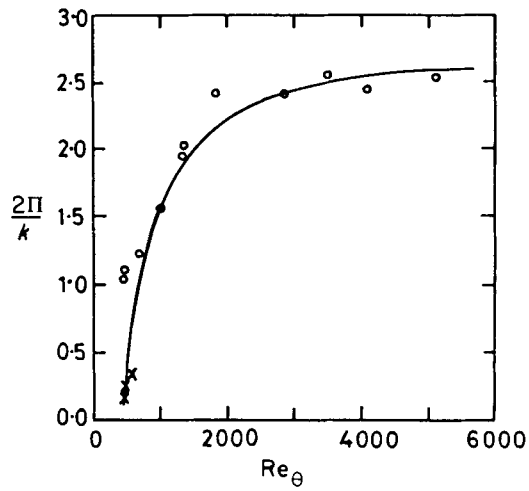

Figure 7. Variation of wake strength $2\Pi/\kappa$ with Reynolds number: ×, present computation; ——, Reference 18; ○, Reference 21

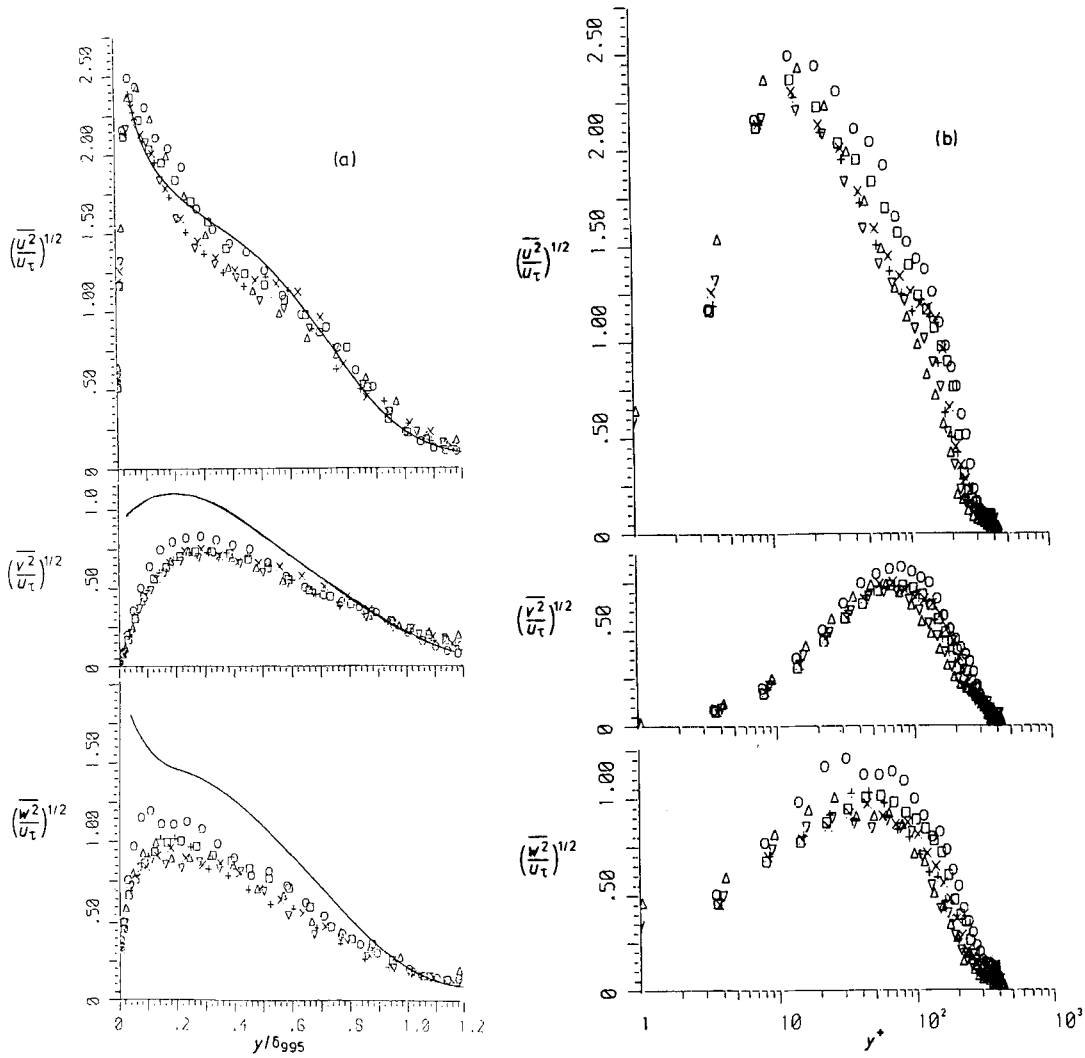

Figure 8. RMS velocity fluctuation profiles, (a) in outer layer co-ordinates and (b) in wall layer co-ordinates Δ, $Re_\theta = 353$; ▽, 396; +, 434; ×, 471; □, 505; ○, 576; ——, Reference 47

The profiles of the resolved scale turbulent intensities are shown in Figures 8(a) and 8(b). Included for comparison are the experimental data of Klebanoff.[47] The profiles presented in the outer layer variables show acceptable overall agreement with experiment in the outer layer. In common with LES work, $(\overline{u^2})^{1/2}$ shows better agreement, while the vertical and spanwise components show greater attenuation near the wall. All these indicate that in the near-wall regions not all the scales of motion are resolved and that significant subgrid scale motions are present and unaccounted for. It is not easy to estimate the subgrid kinetic energy because of the highly anisotropic nature of the mesh near the wall. The data plotted in inner variables are presented in Figure 8(b). As we would expect, the intensities scale on inner variables in the wall region. The peak of $(\overline{u^2})^{1/2}$ is at $y^+ \simeq 20$, which is further away from the wall than the

experimental peak. This is also true for the other components. The LES of the channel flow by Moin and Kim[9] and others show similar features.

The structural parameter u^2v^2 is shown in Figure 9. The general features are as one would expect, with the ratio rising to a very large value near the wall since $\overline{v^2}$ approaches zero faster than $\overline{u^2}$. A local dip at $y/\delta_{995}=0{\cdot}4$ in the current work is also consistent with the low-Reynolds-number experiments of Murlis *et al.*,[22] but their overall values are lower. In contrast with Murlis *et al.* who found values of 1·7–2·3 for the region y/δ_{995} between 0·2 and 0·8, Subramanian and Antonia[23] obtained values around 3·5, in close agreement with ours. All these results indicate that there is no Reynolds number dependence in $\overline{u^2}/\overline{v^2}$.

In order for the subgrid stresses to be proportional to the grid-scale strains, the stresses must be rendered trace-free by transferring the subgrid kinetic energy to the pressure: the grid-scale pressure is thus contaminated with this quantity. The RMS values of this modified pressure are shown in Figure 10(a) and 10(b). It is to be expected that this contamination will be small in the outer layer and will increase towards the wall where the proportion of subgrid energy is larger. Despite this, the RMS pressures presented here are believed to provide a qualitative picture of the intensity and distribution of the pressure. The results show that the RMS value approaches a maximum on the wall where the turbulent kinetic energy is converted to pressure. Since no experimental data are available for pressure fluctuations away from the wall, no comparison could be made there. The full simulation results of Kim *et al.*,[11] however, show the peak RMS to be away from the wall. Thus it would appear that the subgrid-scale models do affect the pressure in the near-wall region. Measurements on the wall are available and are in reasonable agreement with our computation. Various factors such as microphone size and sensitivity affect the measurements, and likewise the simulated results are influenced by grid resolution. The agreement between the results is therefore rather surprising since our grid on the wall is rectangular

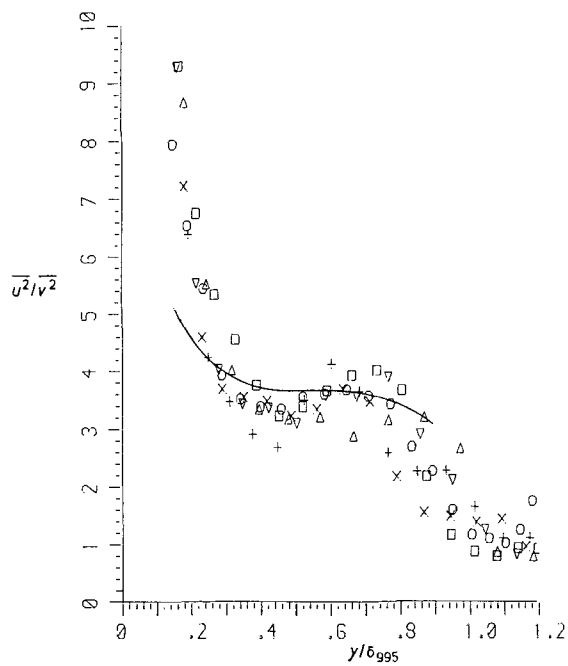

Figure 9. Structure parameter, u^2/v^2, profiles in outer layer co-ordinates: symbols are as in Figure 8; ——, Reference 23

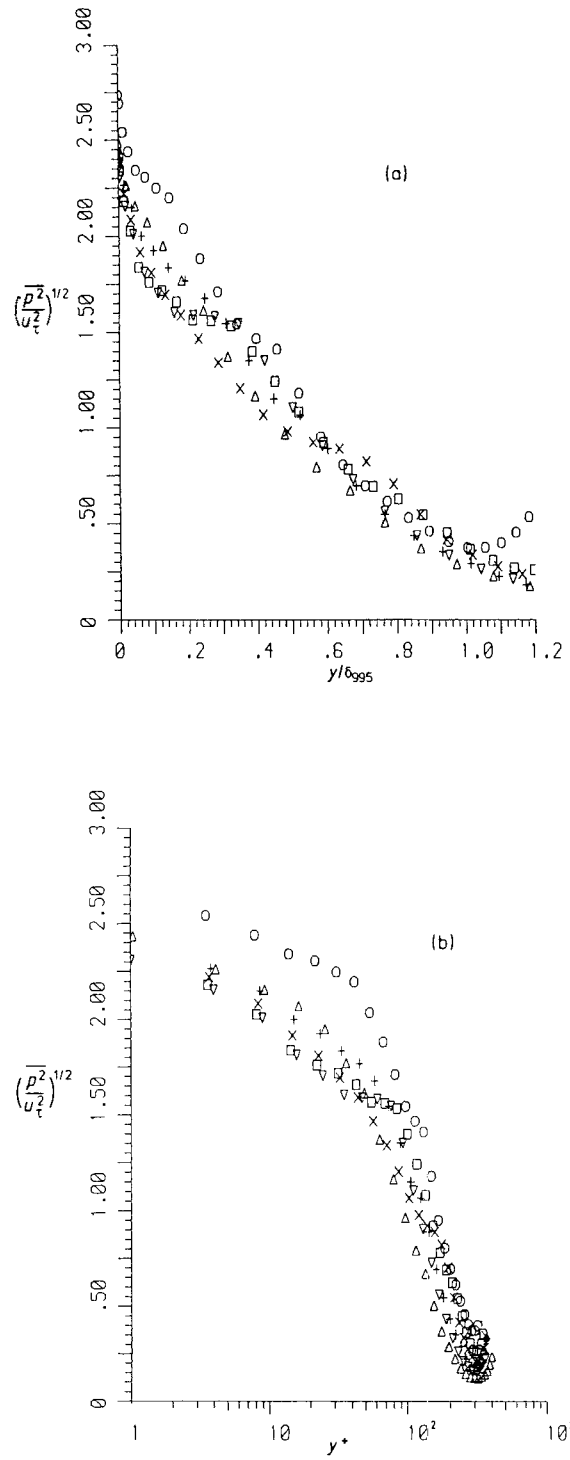

Figure 10. RMS resolvable pressure fluctuation profiles, (a) in outer layer co-ordinates and (b) in wall layer co-ordinates symbols are as in Figure 8

($75 \times 9{\cdot}5\nu/u_\tau$) while the microphones used in the experiment are circular. The experimental value for the RMS wall pressure in units of u_τ^2 using microphones of diameters larger than $100\nu/u_\tau$ varies from 2·31[48] to 2·6[49] and values as high as 3·59 were obtained with more refined instruments which resolve the finer-scale motions.[50].

The overall picture of the pressure distribution is that it peaks on the wall but does not seem to scale on wall variables for the region near the wall (Figure 10(b)). It is generally agreed that the low-wave-number components of the near-wall pressure fluctuations are driven by velocity fluctuations in the outer layer and therefore scale on outer variables; the high-wave-number components are locally driven and scale on wall variables. The pressure spectrum falls fast at high k (perhaps as k^{-3}) and the RMS fluctuations should therefore be dominated by non-local effects. Our results agree with this picture, even though 'low' and 'high' wave numbers are not well separated at the low Re_θ of our simulation. A further complication arises from the change in the scale of the grid resolution as the boundary layer develops in time. As the boundary layer grows, the wall shear decreases; the grid size in wall units also decreases, giving a larger value of resolvable wall pressure fluctuations at the last station considered here. Hence with better resolution the subgrid-scale pressures are better resolved and are therefore better accounted for. This is analogous to having finer measuring transducers in experiments which are found to give higher pressure fluctuation on the wall. These complications make it hard to draw any meaningful conclusions about the Reynolds number dependence of the wall pressure from the present set of results. On the basis of experimental data from measurements with $Re_\theta > 6000$, Bull[51] suggested that the non-dimensionalized RMS wall pressure does increase with Re_θ. There is a hint in Figure 10(a) that this is the case here as well.

Figure 11(a) shows the profiles of the grid-scale turbulent shear stress ($-\overline{uv}$) and of the total turbulent shear stress ($-\overline{uv} - \tau_{12}$): both are non-dimensionalized by u_τ^2. It is clear that the subgrid-scale contribution to the total turbulent stress is substantial only in the near-wall region. The main contributor to τ_{12} is the inhomogeneous component of the subgrid-scale model; in comparison, the homogeneous contribution is barely perceptible. The viscous stress on the wall

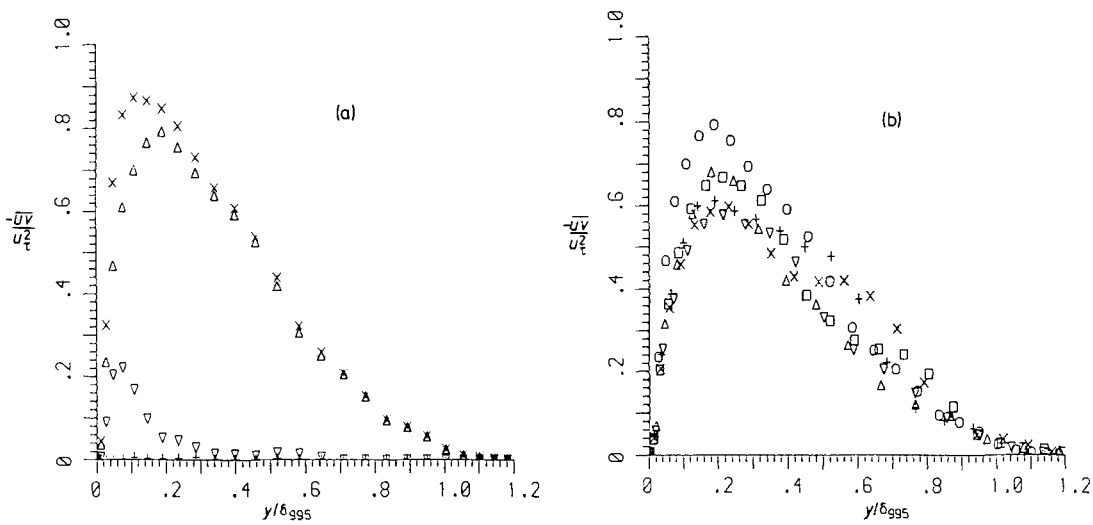

Figure 11. (a) Resolvable and subgrid Reynolds stresses at $Re_\theta = 576$: ×, total; +, homogeneous component of τ_{12}; ▽, inhomogeneous component of τ_{12}; △, resolvable component of the Reynolds stress. (b) Resolvable part of the Reynolds stress at different Re_θ: symbols are as in Figure 8

(which is non-dimensionalized to unity) is about 10% higher than the maximum of the turbulent stresses away from the wall where the viscous contribution is small. Figure 11(b) shows the resolvable scale part of the Reynolds stresses at the various Reynolds numbers. The normalized values do not approximate to unity in the logarithmic region ($0{\cdot}05 < y/\delta_{995} < 0{\cdot}2$) and they do not show good similarity in the outer part of the layer over the range of Re_θ considered here. The peak value of the Reynolds stress is dependent on the Reynolds number; viscous stresses are significant at low Re_θ. This is clearly demonstrated in the comparison of the turbulent channel flows of Eckelmann[43] ($h^+ = 194$), who found a peak Reynolds stress of 0·65, and of Comte-Bellot[34] ($h^+ > 2300$), who found a higher peak value of 0·85. For the low Re_θ which we have simulated, there appears to be some Reynolds number dependency of the peak Reynolds stress. However, the peak Reynolds stress is experimentally found to be independent of Re_θ for values greater than 900.[22,23]

The correlation coefficient $R_{12} \equiv -\overline{uv}/(\overline{u^2}\,\overline{v^2})^{1/2}$ shown in Figure 12(a) indicates that the correlation of the vertical and horizontal fluctuating components is not too dissimilar at differing Re_θ. The present values are in reasonable agreement with the commonly established plateau value of 0·45–0·5.[47] A feature not commonly observed in experiments is the higher correlation as the wall is approached.

In Figure 12(b) the profile of the stress energy ratio a_1 shows considerable scatter in the outer layer ($0{\cdot}3 < y/\delta_{995} < 1{\cdot}0$) between values of 0·13 and 0·23. The average of approximately 0·18 is not too dissimilar to the value of 0·15 established by Bradshaw[52] and Bradshaw and Ferriss.[53]

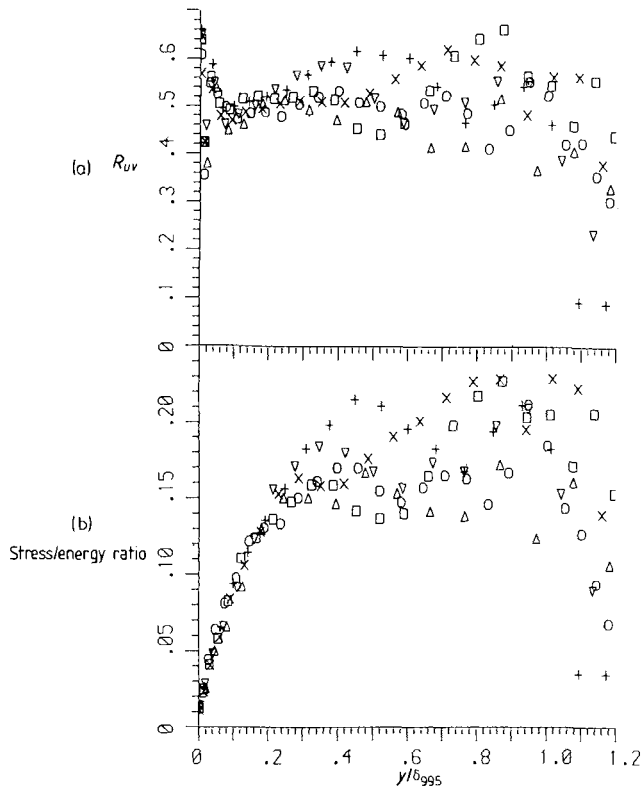

Figure 12. (a) Correlation coefficient $R_{uv} = \overline{uv}/(\overline{u^2}\,\overline{v^2})^{1/2}$ and (b) stress energy ratio $-\overline{uv}/(\overline{u^2}+\overline{v^2}+\overline{w^2})$: symbols are as in Figure 8

The skewness and flatness factors of the fluctuating velocity components, defined as

$$S(u_i) = \frac{\overline{u_i^3}}{(\overline{u_i^2})^{3/2}} \quad \text{and} \quad F(u_i) = \frac{\overline{u_i^4}}{(\overline{u_i^2})^2} \quad (i = 1, 2, 3; \text{ no summation})$$

respectively, are given in Figures 13(a) and 13(b). Also included are similarly defined factors for the pressure fluctuations. The velocity fluctuations have skewness and flatness factors of approximately 0 and 3 respectively in the logarithmic region. At $y/\delta_{995} < 0{\cdot}5$, large changes in these parameters indicate the existence of the turbulent/non-turbulent interface. Nearer to the wall the flatness factors of all the velocity components rise, reflecting the existence of intermittent turbulent structures. The values of $S(u_1)$ are greater than zero in the vicinity of the wall and also in the outer layer; they are slightly less than zero in the logarithmic region. The general behaviour of

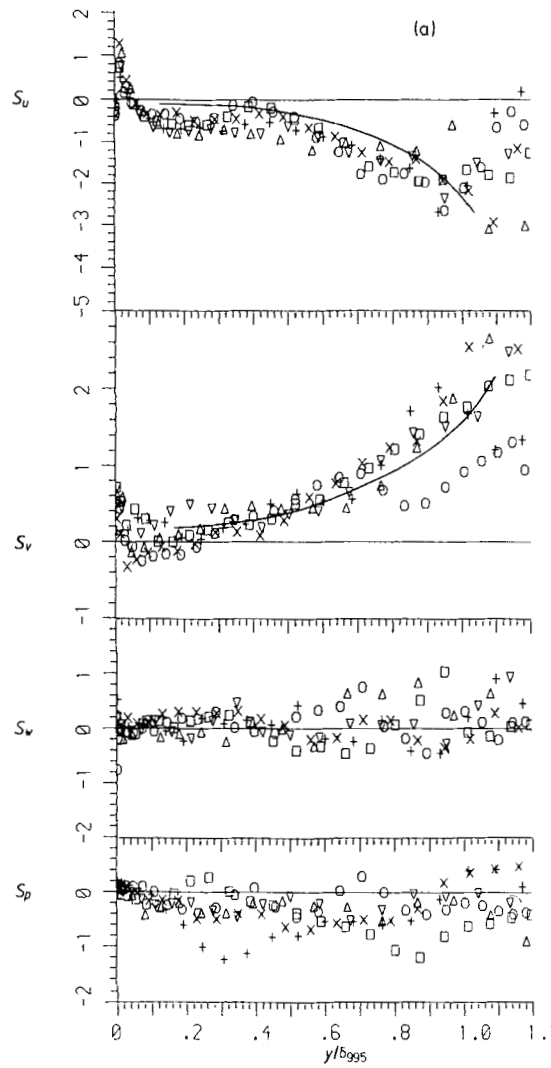

Figure 13(a)

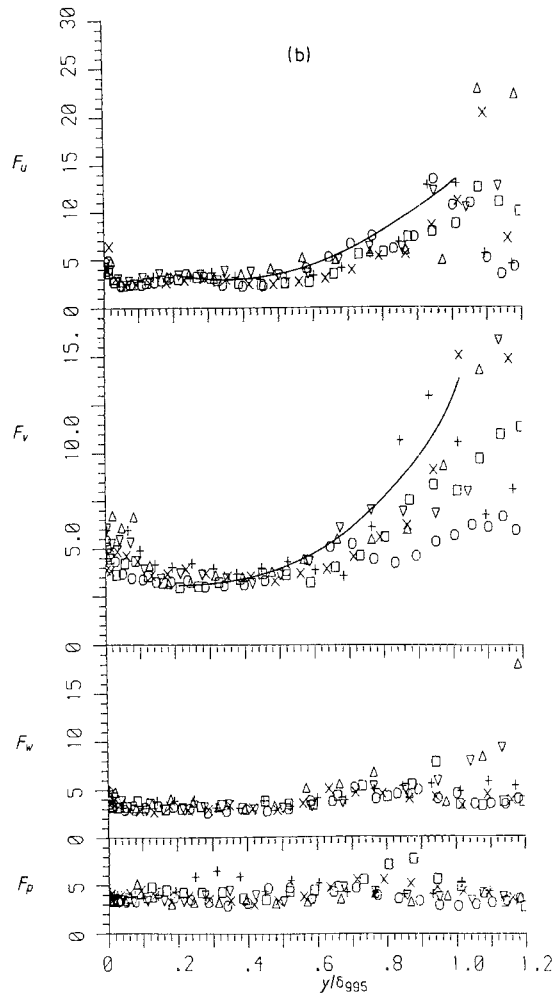

Figure 13. (a) Skewness and (b) flatness factors of u, v, w and p: symbols are as in Figure 8; ——, Reference 54, $Re_\theta = 4680$

these factors is consistent with the measurements of Kreplin and Eckelmann[39] of the near-wall region in a channel flow. In the outer region they agree with those of Hancock[54] who made measurements in a boundary layer. The skewness and flatness factors of the resolvable pressure show basic features similar to those of w in a large part of the layer. However, in the outer region these factors do not rise like those for the velocity fluctuations, reflecting the fact that the pressure field is not as intermittent as the velocity field in the outer layer.

7. TWO-POINT SPATIAL CORRELATIONS AND LENGTH SCALES

The two-point correlations reflect among many other things the adequacy of the computational box size. The streamwise and spanwise correlations R_{ii} at four vertical locations are shown in Figures 14(a) and 14(b) respectively. The separation distances are non-dimensionalized by the boundary layer thickness. The features of correlations near the wall are substantially different

from those taken further out. In the outer region where the flow is intermittent, with turbulent and non-turbulent regions, the scale of the correlations increases progressively. As convincingly demonstrated using conditional measurements by Wood and Bradshaw[55] in a mixing layer and by Tsai[56] in a boundary layer, the increase in spanwise correlations found in the outer region is attributable to the contribution from the non-turbulent flow. At first sight it may seem that the computational box is inadequate in the outer layer since the correlations do not tail sufficiently to zero at the edge. However, noting that most of these are from the non-turbulent portion, which has energy only at the bottom end of the wave number spectra, this is not significant. We are not particularly interested in the behaviour of the non-turbulent part of the flow in so far as it does not seriously affect the bulk of the boundary layer.

Before we interpret the velocity correlations, we will discuss their broad features and relate them to the experimental results of Grant[31] and the simulated results of Moin and Kim.[9] The correlation profiles show that in general the longitudinal correlation in the streamwise direction tails off at a longer distance than the other correlations, while for small separation the correlation whose separation direction is aligned with the velocity is the largest. Note that Grant's results are

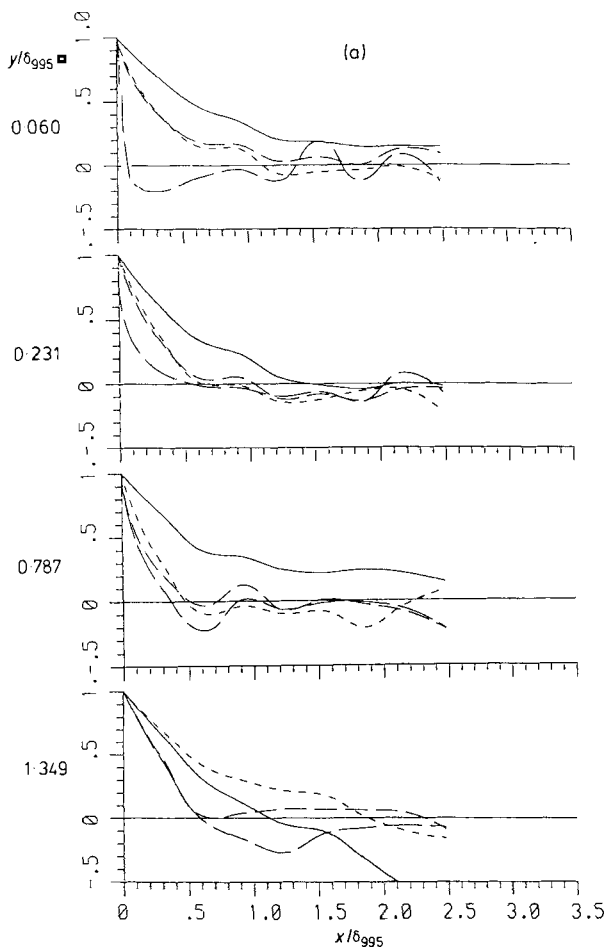

Figure 14(a)

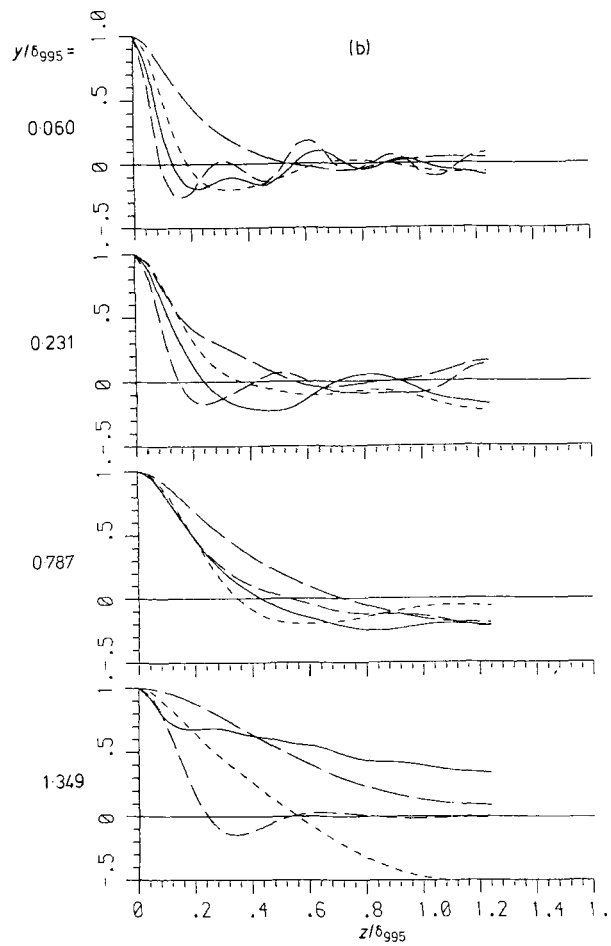

Figure 14. (a) Streamwise and (b) spanwise two-point correlation functions of u, v, w and p at various positions from the wall, $Re_\theta = 505$: ——, R_{11}; – – –, R_{22}; ———, R_{33}; —— ——, R_{pp}

for a boundary layer at $Re_\theta = 1800$, which is 3·5 times greater than our largest Re_θ. Also Grant presented data for separation distances up to one boundary layer thickness only, so that comparisons cannot be made beyond this. Comparison with Moin and Kim's results for a fully developed channel flow is valid for the inner layer only.

The streamwise correlations (Figure 14(a)) of R_{11} $(r, 0, 0)$ remain high over a longer distance, with R_{22} and R_{33} being of the same order for y/δ_{995} less than (say) 0·5, much as in the simulation of Moin and Kim. Agreement with Grant in the outer layer is good, but in the wall region his results differ from ours and from those of Moin and Kim. In view of the difficulties of near-wall measurements and the problems raised by placing one probe in the wake of another to get the streamwise correlations, Grant's results may be in doubt. In the outer region, for y larger than δ_{995}, R_{11} $(r, 0, 0)$ is negative at large separations.

To examine the scale of these correlations, the well known integral scales L_x^u, L_x^v, L_x^w, L_x^p, L_z^u, L_z^v, L_z^w and L_z^p are used, obtained from the zero-wave-number component of the one-dimensional

energy spectra. For example, L_x^u, is defined by

$$\lim_{k_1 \to 0} \frac{E_1(k_1)}{\overline{u^2}} = \frac{2L_x^u}{\pi},$$

where $E_1(k_1)$ is the one-dimensional energy spectrum and k_1 is the x-component wave number. These length scales, expressed as a fraction of the boundary layer thickness, are given in Figures 15(a) and 15(b). The results for the various Reynolds numbers are plotted together. Although there is considerable scatter, the suggestion is that these length scales scale on boundary layer thickness for different Re_θ. In particular, the longitudinal length scale (Figure 15(a)) of the component from R_{11} $(r, 0, 0)$ compares well with the results of Antonia and Luxton,[57] though their Re_θ is about 2000. The longitudinal length scales for the other components, R_{22} and R_{33}, increase away from the wall. No experimental data are available for comparison with these.

The spanwise correlations (Figure 14(b)) are in reasonably good agreement with Grant's even in the near-wall region, the major departure being the larger negative values of the R_{33} $(0, 0, r)$. Except for the length scale of the pressure fluctuations, the spanwise scales are considerably smaller than the longitudinal (Figure 15(b)). Despite the scatter, it is clear that they increase in the outer layer, particularly the R_{11} $(0, 0, r)$ component.

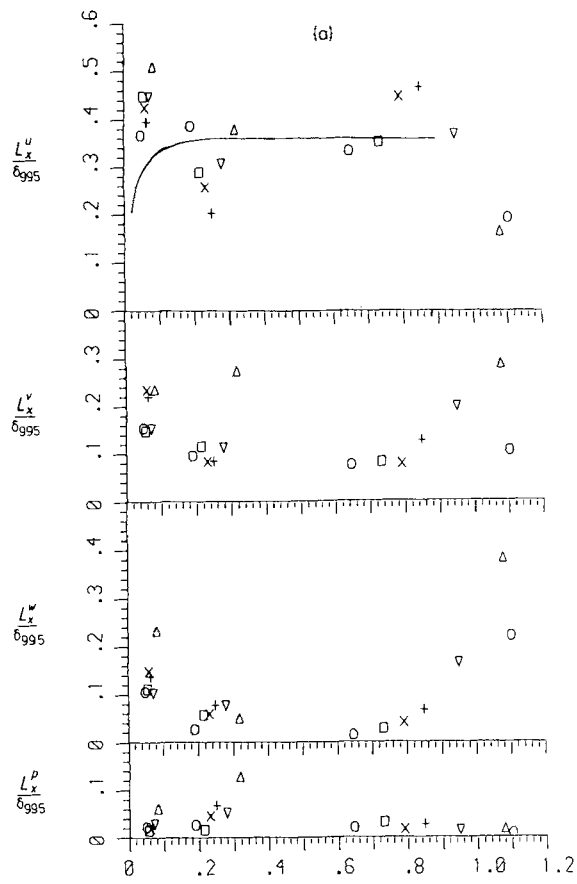

Figure 15(a)

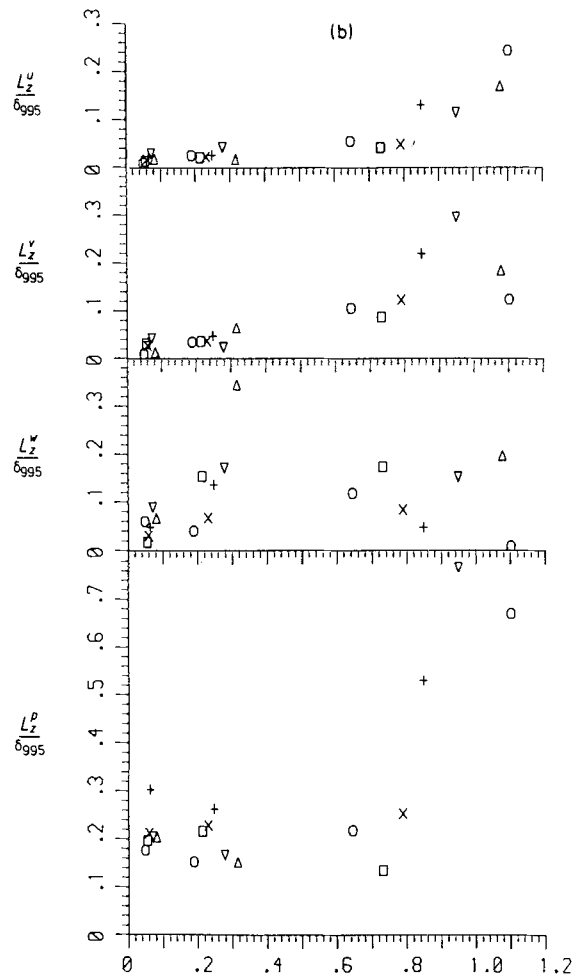

Figure 15. Length scale distribution—(a) streamwise L_x^i and (b) spanwise L_z^i as a function of y/δ_{995} at various Reynolds numbers: symbols are as in Figure 8; ——, Reference 57

Townsend[58,59] interpreted the correlations as implying the presence of double roller eddies in the x–y plane, inclined at 45° to the free stream. The strongest evidence for this is the negative loops in R_{11} (0, 0, r) and R_{33} (0, 0, r). Since the vortex lines must join, the simplest conjecture would be that the structure is horseshoe-like. In the present results (Figure 14(b)) the behaviour of R_{22} (0, 0, r) and R_{33} (0, 0, r) at $y/\delta_{995} = 1{\cdot}349$, where the contributions are primarily from the potential flow motion, is consistent with this, bearing in mind that our Re_θ of about 500 is just the value at which Head and Bandyopadhyay[26] (1981) observed that the dominant features are horseshoe-like structures whose vertical extent is of order δ_{995}. The resemblance of the present correlations to those at higher Re_θ as measured by Grant leads us to conclude that the behaviour of the large-scale structures must be essentially the same at both high and low Reynolds numbers. In particular, it would seem that at large Reynolds numbers the *large-scale* structures which are described by some (e.g. Perry *et al.*[60]) to be an amalgamation of small hairpin vortices and whose size is of the order δ_{995} are in fact also horseshoe-like. Note further that the integral length scales

of these structures at high and low Re_θ scale with boundary layer thickness. This concurs with our general conclusion and is consistent with Murlis *et al.*[22] who deduced that the basic dynamics of the large eddies is independent of Reynolds number; however, their range of Re_θ is from 800 upwards.

The correlations for the pressure field show a different behaviour from those for the velocity. A prominent feature is that the streamwise correlation is much smaller and has a negative loop. On the other hand, the spanwise correlations are larger than those for the velocity. Figure 15(b) shows that the spanwise length scales for the pressure also increase monotonically with distance from the wall in the outer layer and are substantially different in magnitude from the other length scales; they are approximately four times the size of the spanwise velocity length scales.

8. TURBULENT TRANSPORT

The turbulent energy equation and the Reynolds stress equation are

$$\frac{\partial \tfrac{1}{2}\overline{q^2}}{\partial t} = P + D - \varepsilon,$$

$$\frac{\partial(-\overline{uv})}{\partial t} = -P_{12} - D_{12} - \phi_{12} + \varepsilon_{12},$$

where

$$P \text{ (production)} = -\overline{uv}\frac{\partial U}{\partial y},$$

$$D \text{ (diffusion)} = \frac{\partial}{\partial y}(-\tfrac{1}{2}\overline{q^2 v} - \overline{pv} + \overline{u_1 f_{12}} + \overline{u_2 f_{22}} + \overline{u_3 f_{32}}),$$

$$\varepsilon \text{ (dissipation)} = \overline{f_{1k}\frac{\partial u}{\partial x_k}} + \overline{f_{2k}\frac{\partial v}{\partial x_k}} + \overline{f_{3k}\frac{\partial w}{\partial x_k}},$$

$$P_{12} \text{ (production)} = \overline{v^2}\frac{\partial U}{\partial y},$$

$$D_{12} \text{ (diffusion)} = \frac{\partial}{\partial y}(-\tfrac{1}{2}\overline{uv^2} - \overline{pu} + \overline{uf_{22}} + \overline{vf_{12}}),$$

$$\phi_{12} \text{ (pressure–strain)} = \overline{p\left(\frac{\partial u}{\partial y} + \frac{\partial v}{\partial x}\right)},$$

$$\varepsilon_{12} \text{ (dissipation)} = \overline{f_{1k}\frac{\partial u}{\partial x_k} + f_{2k}\frac{\partial v}{\partial x_k}},$$

with

$$f_{ik} = F_{ik} - \langle F_{ik}\rangle,$$

$$F_{ik} = 2(\nu + \nu_t^*)S_{ik} + 2(\nu + \nu_t)(S_{ij} - \langle S_{ik}\rangle).$$

Since the code used for the simulation assumes periodic inflow and outflow conditions, the left-hand sides of the transport equations are the effective advection terms. All the terms on the

right-hand side were evaluated directly, and the advection (here represented as a time derivative) is then found by differencing. Inadequacy of modal representation, forced on us by limitations of computer capacity, makes it impossible to secure precise energy balance at the wall; details of these numerical problems will be reported elsewhere. It seems that they do not invalidate the results obtained in any major quantitative or qualitative manner.

The triple products which appear in the turbulent energy equation and the shear balance equation are presented in Figure 16. As would be expected for higher-order statistics, there is considerable scatter. In any event, triple products do not scale on u_τ, so that collapse of the points on a single curve is not to be expected. The overall trend and shape of these profiles are consistent with experiments. Of the three triple products which appear in the turbulent energy equation ($\overline{u^2v}$, $\overline{v^3}$ and $\overline{w^2v}$), $\overline{v^3}$ and $\overline{w^2v}$ are comparable in magnitude and their peak values are five times

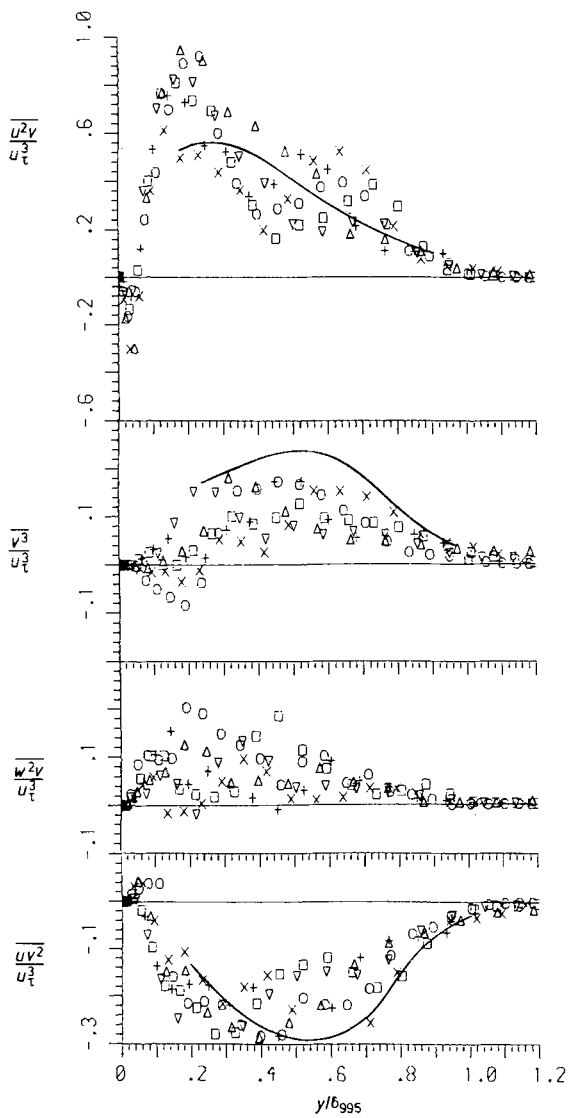

Figure 16. Various triple products normalized by u_τ^3: symbols are as in Figure 8; ——, Reference 22

smaller than that of $\overline{u^2v}$. The $\overline{u^2v}$ profile shows negative values in the wall region, indicating the wallward diffusion of $\overline{u^2}$. This is also found in the measurements of Andreopoulos and Bradshaw.[61] There appears to be a local minimum at $y/\delta_{995} = 0{\cdot}5$ similar to that in the measurements of Murlis *et al.*[22] at Re_θ of 4750. Whether this is a real feature or not is difficult to judge since, as noted earlier, the $\overline{u^2}$ profile shows a slightly larger value in the outer layer (Figure 9). The $\overline{uv^2}$ profile shows similar behaviour to that measured at higher Reynolds number by Murlis *et al.* or Andreopoulos and Bradshaw.

To better assess the behaviour of the turbulent transport of turbulent energy and of shear stress we must also consider the pressure velocity terms $\overline{pv}$ and $\overline{pu}$ (Figure 17). $\overline{pv}$ is comparable in magnitude to the triple-product terms in the turbulent transport equation; as we would expect, its value drops towards the wall. $\overline{pu}$ peaks near the wall and its magnitude is about a third that of $\overline{uv^2}$. Pressure diffusion of $\overline{uv}$ is therefore prominent in the near-wall region in addition to the increasing role of viscous diffusion.

In the outer layer, the magnitudes of advection and diffusion are comparable; the role of viscous diffusion is small. Thus the rate of propagation of turbulent kinetic energy in the

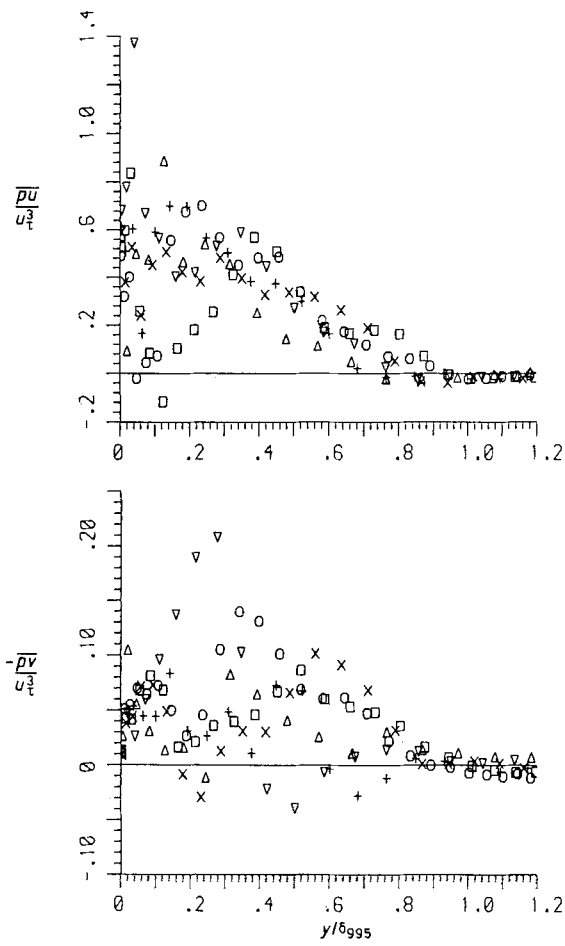

Figure 17. The pressure–velocity pu and pv terms normalised by u_τ^3: symbols are as in Figure 8

cross-stream direction is $\overline{pv}+\frac{1}{2}\overline{q^2v}$, while the rate of propagation of shear stress is $\overline{pu}+\overline{uv^2}$: here $\overline{q^2}\equiv\overline{u^2}+\overline{v^2}+\overline{w^2}$. The transport velocities due to the combined action of pressure and inertial forces are defined by

$$V_q \equiv \frac{\overline{pv}+\frac{1}{2}\overline{q^2v}}{\frac{1}{2}\overline{q^2}} \quad \text{and} \quad V_\tau \equiv \frac{\overline{pu}+\overline{uv^2}}{\overline{uv}}.$$

Since in experimental investigations the pressure–velocity terms are not measured, customary practice is to ignore them. The transport velocities with and without these pressure–velocity contributions are given in Figures 18(a) and 18(b) respectively; the latter are denoted by V'_q and V'_τ. Since $\overline{pv}$ is small, V_q and V'_q are comparable, but V_τ and V'_τ are strikingly different: V'_τ is positive throughout the layer while V_τ is negative near the wall. The comparisons with the transport velocity measurements of, say, Hancock[54] at $Re_\theta = 4680$ for V'_q and V'_τ are reasonable. Since at high Re_θ, $\overline{pu}$ is small, at least in the outer region, we could conclude that the pressure–velocity contribution is important for shear stress transport at low Reynolds number even in the outer layer, at least for the range of Re_θ considered here.

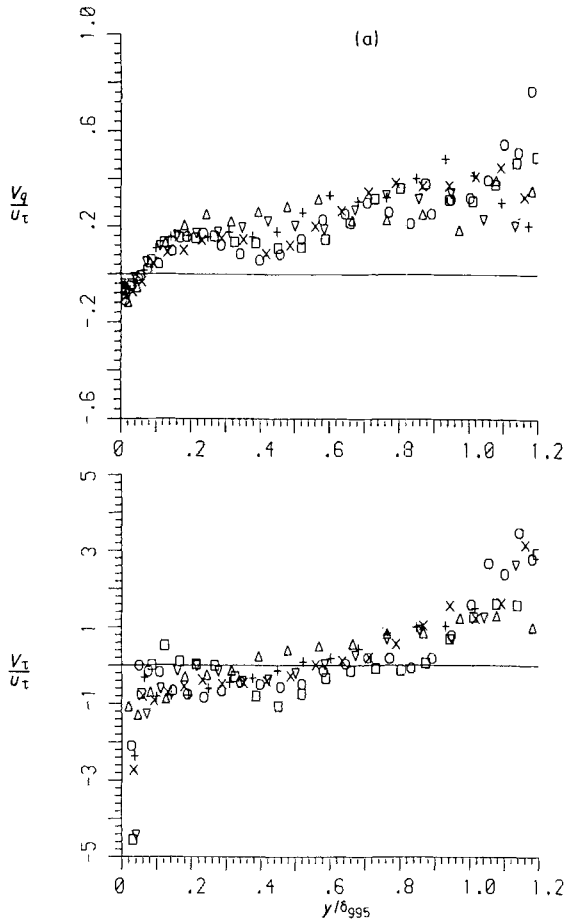

Figure 18(a)

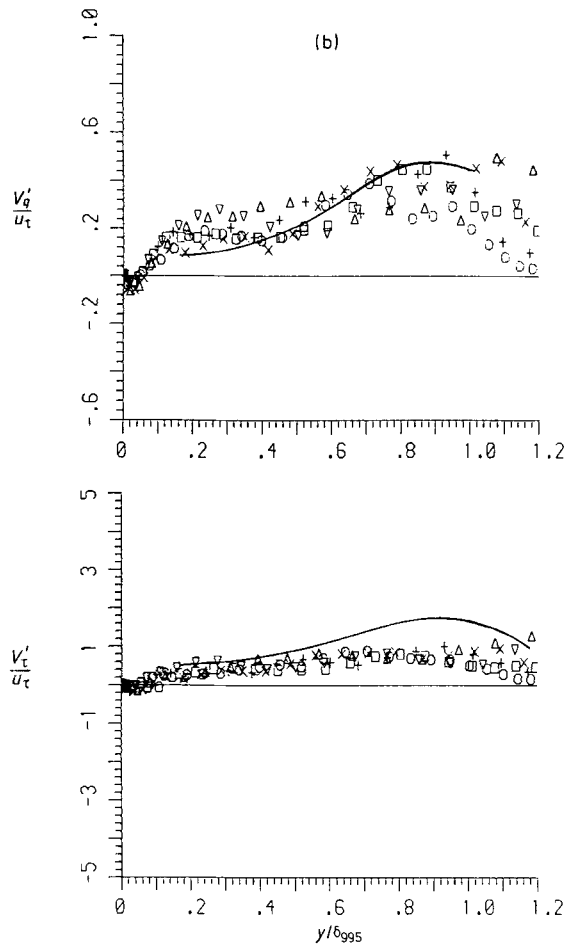

Figure 18. Transport velocity of turbulent energy and shear stress normalized by u_τ, (a) with pressure diffusion contribution and (b) without pressure diffusion: symbols are as in Figure 8; ——, Reference 54

The turbulent kinetic energy balance is given in Figure 19. As one would expect, the results are scattered, in particular the diffusion term since this involves y-derivatives of quantities which are themselves somewhat scattered. Nevertheless, by judicious drawing of lines through these data we can examine the behaviour of the terms. The subgrid dissipation is small beyond a y/δ_{995} of 0·6 and increases to a maximum at about $y/\delta_{995} = 0{\cdot}1$. Molecular viscous dissipation dominates in the near-wall region. On the wall, viscous diffusion is equal in magnitude but opposite in sign to the viscous dissipation. The diffusion changes sign twice in the region $y/\delta_{995} < 0{\cdot}4$. The overall pattern here is similar to the LES results of Moin and Kim.[41] In the outer region, diffusion and advection are important. The conclusion of Murlis *et al.* that diffusion is strong at low Re_θ is clearly borne out in the present results. Here the point at which diffusion equals production is at about $y/\delta_{995} = 0{\cdot}7$, compared to 0·72 and 0·82 for $Re_\theta = 800$ and 4750 respectively as found by Murlis *et al.* Spalart's[14] results for a constant pressure flow at $Re_\theta \approx 600$ are qualitatively the same as the present ones, though his results show a plateau region around $y/\delta = 0{\cdot}8$ for the diffusion. The point where this diffusion equals the production is at about $y/\delta = 0{\cdot}78$. No near-wall results are given for comparison here.

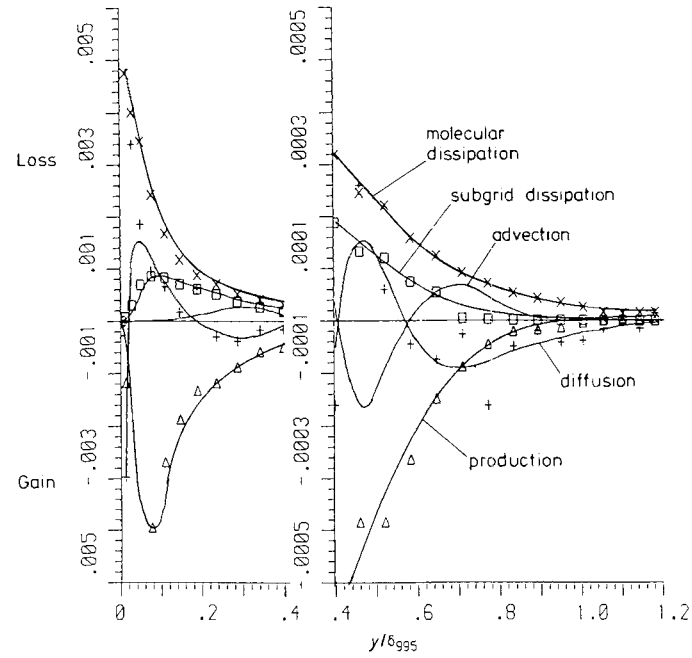

Figure 19. Resolvable turbulent energy balance normalized by δ_{995}/U_e^3 at $Re_\theta = 576$ (note change in scale)

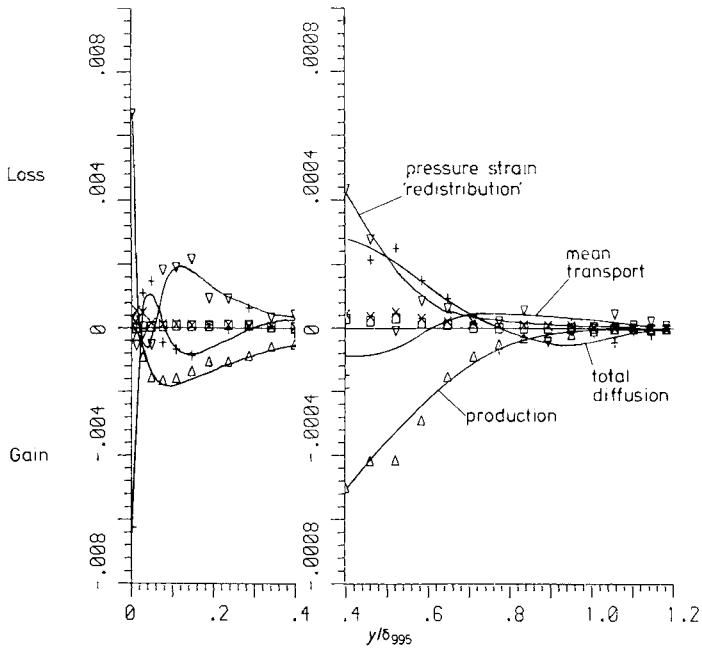

Figure 20. Resolvable shear stress balance normalized by δ_{995}/U_e^3 at $Re_\theta = 576$ (note change in scale)

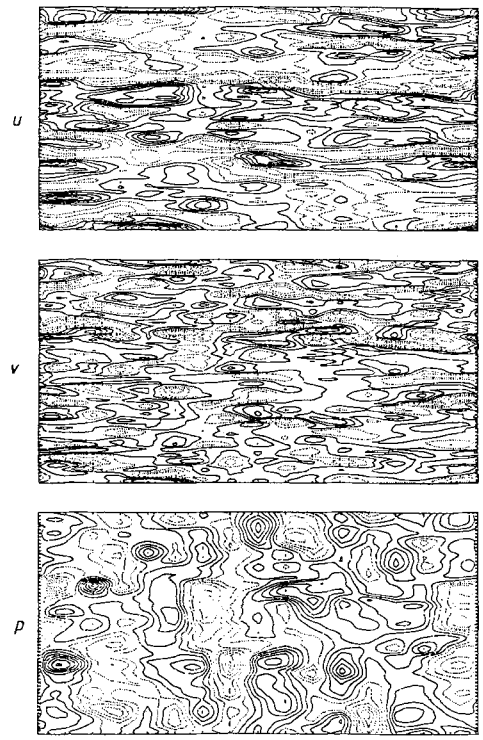

Figure 21. Contours of fluctuating u, v and p in the x–z plane at $Re_\theta = 535$ and $y^+ = 3{\cdot}5$

Figure 20 shows the variation with y/δ_{995} of the various terms in the balance equation for the Reynolds stress at $Re_\theta = 576$; note the change of scale near the wall. The most outstanding feature is that the dissipation term ε_{12} is small and indeed almost insignificant. The dissipation of the shear stress must tend to zero as $Re \to \infty$ because its inertial range spectrum is then $O(k^{-7/3})$. (Reference 62, p. 322), but it is not obvious that it will be small even at such low Reynolds numbers. The subgrid and viscous contributions are roughly equal in magnitude.

In the virtual absence of dissipation, pressure–strain is the main destruction mechanism (note that in Figure 20 a positive sign indicates the destruction of stress). The pressure–strain is positive except for a small sign reversal near the wall. It is balanced by viscous diffusion near the wall. In the outer regions both pressure–strain and dissipation are small, and the energy injected by diffusion is mainly removed by advection. (As in the turbulent kinetic energy balance, advection is represented by a purely temporal change.) The diffusion changes signs no less than four times. It is of course predominantly viscous diffusion near the wall; further out, diffusion is mainly due to turbulent effects, but pressure effects are also important, at least at the Re_θ we are simulating here.

It is in principle possible to extend the simulation to higher Re_θ by using synthetic rather than natural boundary conditions, but we have not done this. For the moment, working from experimental data, we see that the effect of increasing Re_θ is to diminish diffusion and all effects other than production and pressure–strain. The stress is then determined by the balance between these two effects and the situation becomes not unlike that in the classical high-Reynolds-number homogeneous strain experiment of Champagne *et al.*[63] To supplement this experimental information, the simulation confirms the role of the pressure fluctuations.

9. INSTANTANEOUS FLOW PATTERNS

Figures 21 and 22 show isotachs (contours of constant velocity) of u and v, and isobars, in x–z planes parallel to the wall. The contours in Figure 21 are for $y^+ = 3{\cdot}51$ and they are very similar to those from earlier channel simulations (e.g. Reference 9), with the important difference that here the streak spacings are better resolved. The isobar plots of Figure 21 are much less elongated than the isotachs, and this is consistent with the experimental finding that the two-point correlations of p on the wall are similar in the x- and z-directions. It is particularly striking that this result is achieved in spite of the gross asymmetry of the computational mesh $\Delta x^+ = 76$, $\Delta z^+ = 9$.

Figure 22 shows contours in the plane at $y^+ = 182$, $y/\delta = 0{\cdot}685$ near the outer edge of the boundary layer. It will be seen that the velocity contours are much less elongated than they are near the wall. The most interesting feature is the island of relatively low activity near the centre of all three diagrams. This is presumed to represent the irrotational fluid. The subsequent process of entrainment of this fluid is embodied in these data but has not yet been analysed in detail. The pressure island is less clearly defined than those in the velocity plots, as would be expected from the action-at-a-distance nature of the pressure force.

Figure 23 shows contours in the x–y plane. (The mean velocity has not been removed from the u-plot, and in the v-plot the dashed lines represent outward motion while the solid lines denote wallward motion.) The fluctuations in u at the edge and in the free stream region are small and are not noticeable since the contour intervals are large. The v-fluctuations show up clearly because there is no mean motion to conceal them. The u-plot shows clear evidence of low-speed fluid

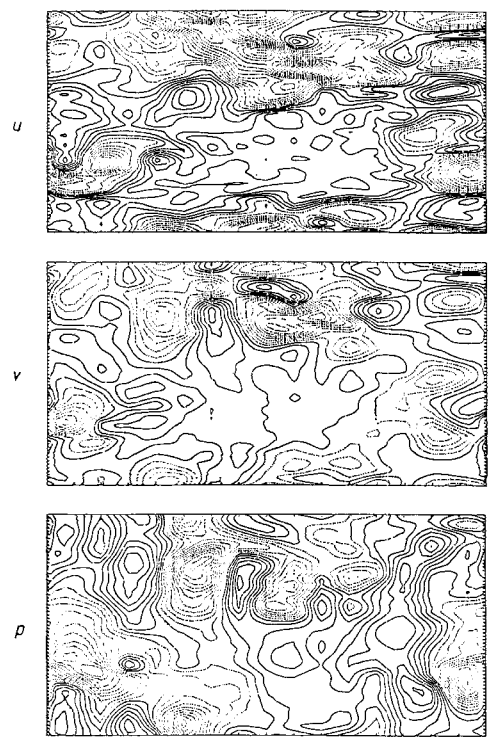

Figure 22. Contours of fluctuating u, v and p in the x–z plane at $Re_\theta = 535$ and $y^+ = 182$, $y/\delta = 0{\cdot}684$

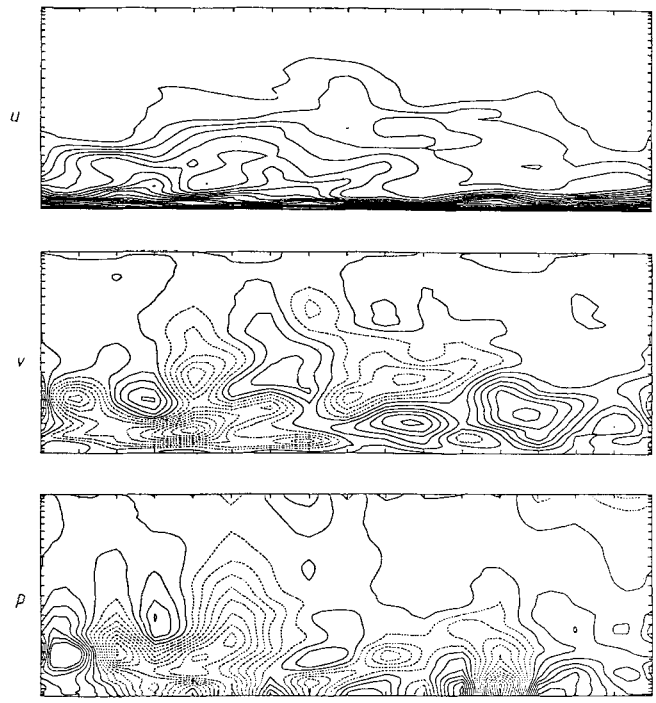

Figure 23. Contours of fluctuating u, v and p in the x–y plane at $Re_\theta = 535$

being advected outwards at an angle to the mean flow, and of high-speed fluid coming inwards in consequence, probably by pressure forces, at the leeward side of the low-speed bulge. The v-plot shows an outward motion sandwiched between two wallward motions. The pressure is, as one would expect, high under regions of incoming fluid (splat) and low under outgoing regions.

Finally, Figure 24 shows plots in the y–z plane, i.e. looking downstream. The near-wall structures are again similar to those found by Moin and Kim,[9] while here the outer region with the irrotational fluid is clearly discernible. The distance between two regions of low-speed streaks is about 180 wall units. It is interesting that between two such low-speed regions the v-contour shows a wallward region with high u-momentum. This is suggestive of the legs of the hairpin vortices, with the outward low-momentum region being the co-flow between the legs of the hairpin. Through viscous action, some of the irrotational fluid is entrained by the movement of the hairpin legs.

10. CONCLUSIONS

We have simulated a low-Reynolds-number boundary layer; this is homogeneous in the streamwise direction and grows outwards with time, but approximates very well to a spatially growing boundary layer. The starting field was generated somewhat artificially using a conditionally sampled field from a previous channel flow simulation. The structures of this starting field are consistent with experimental findings. The development of the boundary layer, and in particular that of the outer layer, behaves normally, although no special measures were taken to model the interface between turbulent and non-turbulent regions. Also, the subgrid model of Moin and Kim[9] was found to be entirely satisfactory. The dominant contribution to the subgrid-scale stress

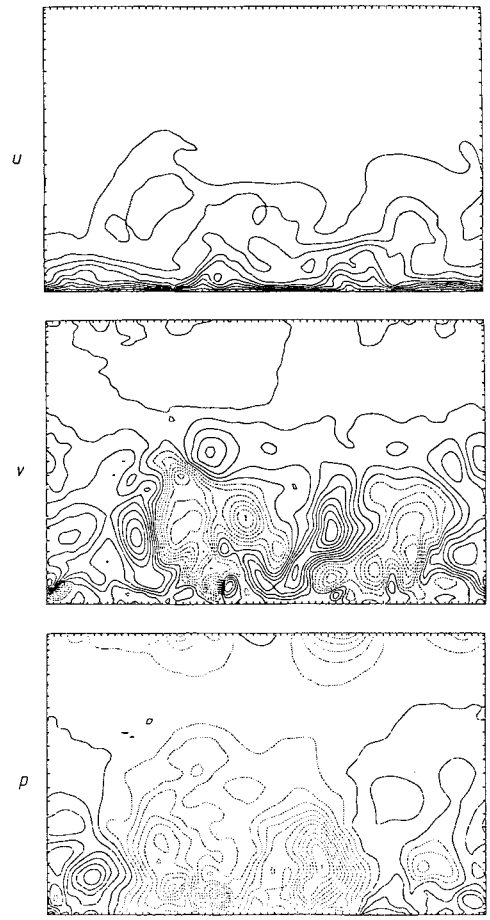

Figure 24. Contours of fluctuating u, v and p in the y–z plane at $Re_\theta = 535$

comes from the inhomogeneous term, while the dissipation of turbulent kinetic energy is solely due to the homogeneous term.

The simulation agrees very well with experiment, and one can therefore have some confidence in its prediction of quantities which have not yet been measured. The most important of these are functions of the fluctuating pressure, such as pressure–strain and pressure–diffusion, and also the two-point correlations which have been measured at high Re only; the simulation therefore extends the range of information on low-Re boundary layers. It has been demonstrated that the calculated correlations are consistent with the presence of horseshoe structures, as is made evident in the flow visualization of Head and Bandyopadhyay[26] at similar Re_θ. Since these correlations are also similar to Grant's[31] measurements at $Re_\theta = 1800$, the implication is that even at higher Re_θ the large-scale structures are also horseshoe-like.

The findings of Murlis *et al.*[22] as to the trend of the energy balance with Re are confirmed by the simulation: in particular, the importance of diffusion diminishes as Re_θ is increased. Similar trends were observed in the shear stress balance; as Re_θ increases, the stress is increasingly determined by a balance between pressure–strain and production. The computed pressure

transport of shear stress was found to be important even in the outer layer; overall, the pressure diffusion of shear stress is important, at least over the range of Re_θ considered here.

Near the wall, the flow structures are similar to those found in studies of channel flows. Synthetic boundary conditions are known to work well for channel flows, and this agreement is encouraging evidence that such conditions will be equally effective for boundary layers. Extension to Reynolds numbers higher than those attempted here should therefore be possible.

The full potential of the simulated field has yet to be investigated. Further studies of the structure of the boundary layer, such as the causal relationships of the various flow modules and the behaviour of the hairpin vortices in the outer layer, similar to those made by Moin and Kim[41] for channel flows, could be made. Of particular interest would be the entrainment process in the outer layer.

ACKNOWLEDGEMENTS

We are grateful to Dr. B. A. Splawski (now of Thermal Hydraulics Division, AERE, Harwell) who developed the CHANEL code (the ancestor of BUOYAN-77) first started by Professor M. Antonopoulos-Domis (now of Aristotelian University of Thessaloniki). Mr. K. A. Cliffe (of Theoretical Physics Division, Harwell) speeded up the code considerably for the CRAY-lS. We wish to acknowledge helpful discussions with Professor P. Bradshaw F.R.S., Stanford University and Dr. P. R. Voke, Queen Mary Westfield College and also comments from the referees which improved the paper. This work is supported by the U.K. Science and Engineering Research Council.

REFERENCES

1. N. N. Mansour, J. H. Ferziger and W. C. Reynolds, 'Large eddy simulation of a turbulent mixing layer', *Report TF-11*, Department of Mechanical Engineering, Stanford University, 1978.
2. J. J. Riley and R. W. Metcalfe, 'Direct numerical simulation of a perturbed, turbulent mixing layer', *AIAA Paper 80-0274*, 1980.
3. A. B. Cain, W. C. Reynolds and J. H. Ferziger, 'A three-dimensional simulation of transition and early turbulence in a time-developing mixing layer', *Report TF-14*, Department of Mechanical Engineering, Stanford University, 1981.
4. S. A. Orszag and Y. Pao, 'Numerical computation of turbulent shear flows', *Adv. Geophys.*, **18A**, 225 (1974).
5. J. J. Riley and R. W. Metcalfe, 'Direct numerical simulations of the turbulent wake of an axisymmetric body', in L. J. S. Bradbury *et al.* (eds). *Turbulent Shear Flows II*, Springer, Berlin, 1980, pp. 78–93.
6. J. W. Deardorff, 'A numerical study of three-dimensional turbulent channel flow at large Reynolds numbers', *J. Fluid Mech.*, **41**, 453 (1970).
7. U. Schumann, 'Subgrid scale model for finite difference simulations of turbulent flows in plane channels and annuli', *J. Comput. Phys.*, **18**, 376 (1975).
8. P. Moin, W. C. Reynolds and J. H. Ferziger 'Large eddy simulation of incompressible turbulent channel flow', *Report TF-12*, Department of Mechanical Engineering, Stanford University, 1978.
9. P. Moin and J. Kim, 'Numerical investigation of turbulent channel flow', *J. Fluid Mech.*, **118**, 341 (1982).
10. S. Gavrilakis, H. M. Tsai, P. R. Voke and D. C. Leslie, 'Large eddy simulation of low Reynolds number channel flow by spectral and finite difference methods', in U. Schumann and R. Friedrich (eds), *Direct and Large eddy Simulation of Turbulence; Proc. EUROMECH Colloq, No. 199*, Vieweg, Braunschweig/Wiesbaden, 1986.
11. J. Kim, P. Moin and R. Moser, 'Turbulence statistics in fully developed channel flow at low Reynolds number', *J. Fluid Mech.*, **172**, 133 (1987).
12. P. R. Spalart, 'Numerical simulation of boundary-layer transition', *NASA Technical Memorandum 85984*, 1984.
13. P. R. Spalart and A. Leonard, 'Direct numerical simulation of equilibrium turbulent boundary layers', in F. Durst *et al.* (eds), *Turbulent shear Flows V*, Springer, Berlin, 1986.
14. P. R. Spalart, 'Numerical study of sink flow boundary layers', *J. Fluid Mech.*, **172**, 133 (1986).
15. R. Friedrich and M. D. Su, 'Large eddy simulation of a turbulent wall bounded shear layer with longitudinal curvature', in E. Krause (ed.), *Proc. Int. Conf. on Numerical Methods in Fluid Dynamics; Lecture Notes in Physics, Vol.170*, Springer, Berlin, 1982, pp. 196–202.
16. L. Schmitt, K. Richter and R. Friedrich, 'Large eddy simulation of turbulent boundary layer and channel flow at high Reynolds number', U. Schumann and R. Friedrich (eds), *Direct and Large eddy simulation of Turbulence; Proc. EUROMECH colloq. No. 199*, Vieweg, Braunschweig/Wiesbaden, 1986.

17. A. A. Wray, M. Y. Hussaini and D. Degani, 'Numerical simulation of transition of turbulence', in E. H. Hirschel and W. Geller (eds), *Proc. 2nd GAMM Conf. on Numerical Methods in Fluid Mechanics*, DEVLR, Köln, 1977, pp. 247–254.
18. D. E. Coles, 'The turbulent boundary layer in a compressible fluid', *Rand Report R403-PR, ARC24473*, 1962, Appendix A.
19. D. E. Coles and E. A. Hirst (eds), *Proc. 1968 AFOSR–IFP Stanford Conf. on Computation of Turbulent Boundary Layers*, Thermosciences Division, Stanford University, 1969.
20. G. D. Huffman and P. Bradshaw, 'A note on the von Karman's constant in low Reynolds number turbulent flows', *J. Fluid Mech.*, **53,** 45 (1972).
21. L. P. Purtell, P. S. Klebanoff and F. T. Buckley, 'Turbulent boundary layers at low Reynolds numbers', *Phys. Fluids*, **24,** 802–811 (1981).
22. J. Murlis, H. M. Tsai and P. Bradshaw, 'The structure of turbulent boundary layers at low Reynolds numbers', *J. Fluid Mech.*, **122,** 13 (1982).
23. C. S. Subramanian and R. A. Antonia, 'Effect of Reynolds number on a slightly heated turbulent boundary layer', *Int. J. Heat Mass Transfer*, **24,** 1833–1846 (1981).
24. R. E. Falco, 'Some comments on turbulent boundary layer structure inferred from the movements of a passive contaminant', AIAA paper 74/99, 1974.
25. R. E. Falco, 'Coherent motions in the outer regions of turbulent boundary layers', *Phys. Fluids Suppl.*, **20,** S124 (1975).
26. M. B. Head and P. Bandyopadhyay, 'New aspects of turbulent boundary layer structures', *J. Fluid Mech.*, **107,** 297 (1981).
27. M. Antonopoulos-Domis, 'Numerical simulation of turbulent flows in plane channels', *Proc. Third Int. Conf. on Numerical Methods in Laminar and Turbulent Flows*, Pineridge Press, Swansea, 1983, pp. 113–123.
28. P. R. Voke, H. M. Tsai and M. W. Collins, 'The use of chebyshev polynomials in spectral fluid dynamics simulations', in K. W. Morton and M. J. Baines (eds), *Numerical Methods for fluid Dynamics II*, Clarendon Press, Oxford, 1985, p. 477.
29. J. Leray, 'Essai sur le mouvement d'un liquide visqueux emplissant l'espace', *Acta Math.*, **63,** 193 (1934).
30. A. Leonard and A. Wray, 'A new numerical method for simulation of three-dimensional flow in a pipe', in E. Krause (ed.), *Proc. Int. Conf. on Numerical Methods in Fluid Dynamics; Lecture Notes in Physics, Vol. 170*, Springer, Berlin, 1982, pp. 335–342.
31. H. L. Grant, 'The large eddies of turbulent motion', *J. Fluid Mech.*, **4,** 149 (1958).
32. D. J. Tritton, 'Some new correlation measurements in a turbulent boundary layer', *J. Fluid Mech.*, **28,** 439 (1967).
33. D. R. Moser, 'Direct numerical simulation of curved turbulent channel flow', *Ph.D. Dissertation*, Stanford University, 1984.
34. G. Comte-Bellot, 'Contribution a l'étude de la turbulence de conduite', *Doctoral Thesis*, University of Grenoble, 1963.
35. P. Bradshaw, 'The effect of initial conditions on the development of a free shear layer', *J. Fluid Mech.*, **26,** 225 (1966).
36. C. Chandrsuda, R. D. Mehta, A. D. Weir and P. Bradshaw, 'Effect of free-stream turbulence on large structure in turbulent mixing layers', *J. Fluid Mech.*, **85,** 693–704 (1978).
37. R. B. Dean and P. Bradshaw, 'Measurements of interacting shear layers in a duct', *J. Fluid Mech.*, **78,** 641 (1976).
38. A. D. Weir, D. H. Wood and P. Bradshaw, 'Interacting turbulent shear layers in a plane jet', *J. Fluid Mech.*, **107,** 237 (1981).
39. H. Kreplin and M. Eckelmann, 'Behaviour of the three fluctuating velocity components in the wall region of a turbulent channel flow', *Phys. Fluids*, **22,** 1233 (1979).
40. J. Sternberg, 'On the interpretation of space–time correlation measurements in shear flow', *Phys. Fluids Suppl.*, **10,** S146 (1967).
41. P. Moin, and J. Kim, 'The structure of the vorticity field in turbulent channel flow. Part 1. Analysis of instantaneous fields and statistical correlations', *J. Fluid Mech.*, **155,** 441 (1985).
42. L. Landweber, 'The frictional resistance of flat plates in zero pressure gradient', *Trans. SNAME*, **61,** 5–32 (1953).
43. H. Eckelmann, 'The structure of the viscous sublayer and the adjacent wall region in a turbulent channel flow', *J. Fluid Mech.*, **65,** 439–59 (1974).
44. P. S. Klebanoff and Z. W. Diehl, *NACA Technical Report No. 2475*, 1951.
45. D. G. Mabey, 'Influence of the wake component on turbulent skin friction at subsonic and supersonic speed', *Aero. Q.*, **30,** 590 (1979).
46. I. P. Castro 'Effects of free stream turbulence on low Reynolds number boundary layers', *Trans. ASME J. Fluid Eng.*, **106,** 298–306 (1984).
47. P. S. Klebanoff, 'Characteristics of turbulence in a boundary layer with zero pressure gradient', *NACA Technical Report No. 1247*, 1955.
48. W. W. Willmarth and F. W. Ross, 'Resolution and structure of the wall pressure fluctuations beneath a turbulent boundary layer', *J. Fluid Mech.*, **22,** 81 (1965).
49. J. A. Elliot, 'Microscale pressure fluctuations measured within the lower atmospheric boundary layer', *J. Fluid Mech.*, **53,** 351 (1972).
50. W. W. Willmarth, 'Pressure fluctuations beneath turbulent boundary layers', *Ann. Rev. Fluid Mech.*, **7,** 13 (1975).
51. M. K. Bull, 'Wall pressure fluctuations in turbulent boundary layers', *J. Fluid Mech.*, **30,** 241 (1967).
52. P. Bradshaw, 'The turbulence structure of equilibrium boundary layers', *J. Fluid Mech.*, **29,** 625–646 (1967).
53. P. Bradshaw and D. H. Ferriss, 'Applications of a general method of calculating turbulent shear layers', *Trans. ASME J. Basic Eng.*, **94d,** 345–353 (1972).

54. P. E. Hancock, 'The effects of free stream turbulence on turbulent boundary layer', *Ph.D. Thesis*, Imperial College, London, 1980.
55. D. H. Wood and P. Bradshaw, 'A turbulent mixing layer constrained by a solid surface. Part 1. Measurements before reaching the surface', *J. Fluid Mech.*, **122,** 57–89 (1982).
56. H. M. Tsai, 'Some experimental contributions to the study of large eddy structures in turbulent layers', *Ph.D. Thesis*, Imperial College, London, 1987.
57. R. A. Antonia and R. E. Luxton, 'The response of a turbulent boundary layer to a step change in surface roughness. Part 1. Smooth to rough', *J. Fluid Mech.*, **48,** 721 (1971).
58. A. A. Townsend, 'Entrainment and the structure of turbulent flow', *J. Fluid Mech.*, **41,** 13–46 (1970).
59. A. A. Townsend, *The Structure of Turbulent Shear Flow*, 2nd edn, Cambridge University Press, 1976.
60. A. E. Perry, S. M. Henbest and M. S. Chong, 'A theoretical and experimental study of wall turbulence', *J. Fluid Mech.*, **165,** 163–199 (1986).
61. J. Andreopoulos and P. Bradshaw, 'Measurements of interacting turbulent shear layers in the near wake of a flat plate', *J. Fluid Mech.*. **100,** 639 (1980).
62. D. C. Leslie, *Developments in the Theory of Turbulence*, Clarendon Press, Oxford, 1973.
63. F. H. Champagne, V. G. Harris and S. Corrsin, 'Experiments on nearly homogeneous turbulent shear flow', *J. Fluid Mech.*, **41,** 81 (1970).